European Journal of Medicinal Chemistry 45 (2010) 1598–1617

Contents lists available at ScienceDirect

European Journal of Medicinal Chemistry

journal homepage: http://www.elsevier.com/locate/ejmech

Original article

Discovery of new cholesteryl ester transfer protein inhibitors via ligand-based pharmacophore modeling and QSAR analysis followed by synthetic exploration

Reema Abu Khalaf [a], Ghassan Abu Sheikha [a], Yasser Bustanji [b], Mutasem O. Taha [c,*]

[a] Faculty of Pharmacy, Al-Zaytoonah Private University of Jordan, Amman, Jordan
[b] Department of Biopharmaceutics and Clinical Pharmacy, Faculty of Pharmacy, University of Jordan, Amman, Jordan
[c] Department of Pharmaceutical Sciences, Faculty of Pharmacy, University of Jordan, Amman, Jordan

ARTICLE INFO

Article history:
Received 20 July 2009
Received in revised form
16 December 2009
Accepted 23 December 2009
Available online 14 January 2010

Keywords:
CETP inhibitors
In silico screening
Pharmacophore modeling
Quantitative Structure–activity relationship
Shape constraints
Receiver-operating characteristic

ABSTRACT

Cholesteryl ester transfer protein (CETP) is involved in trafficking lipoprotein particles and neutral lipids between HDL and LDL and therefore is considered a valid target for treating dyslipidemic conditions and complications. Pharmacophore modeling and quantitative structure–activity relationship (QSAR) analysis were combined to explore the structural requirments for potent CETP inhibitors. Two pharmacophores emerged in the optimal QSAR equation ($r^2 = 0.800$, $n = 96$, $F = 72.1$, $r^2_{LOO} = 0.775$, r^2_{PRESS} against 22 external test inhibitors $= 0.707$) suggesting the existence of at least two distinct binding modes accessible to ligands within CETP binding pocket. The successful pharmacophores were complemented with strict shape constraints in an attempt to optimize their receiver-operating characteristic (ROC) curve profiles.

The validity of our modeling approach was experimentally established by the identification of several CETP inhibitory leads retrieved *via in silico* screening of the National Cancer Institute (NCI) list of compounds and an *in house* built database of drugs and agrochemicals. Two hits illustrated low micromolar IC_{50} values: NSC 40331 ($IC_{50} = 6.5$ μM) and NSC 89508 ($IC_{50} = 1.9$ μM). Active hits were then used to guide synthetic exploration of a new series of CETP inhibitors.

1. Introduction

Atherosclerosis describes the principal progression in arterial dysfunction and remodeling that restricts blood flow to vessels in the peripheral vasculature and is ultimately manifested as coronary artery disease (CAD) [1]. Several epidemiological studies have demonstrated an inverse relationship between serum high-density lipoprotein cholesterol (HDLc) levels and the incidence of ischemic heart disease [2]. HDL mediates the reverse cholesterol transport pathway which removes excess cholesterol from peripheral tissues to the liver for biliary elimination [3].

CETP, a 476-residue glycoprotein, is involved in trafficking lipoprotein particles and neutral lipids, including cholesteryl esters (CE), phospholipids and triglycerides between HDL and low-density lipoproteins (LDL). CETP, as revealed by X-ray crystallography (PDB code: 2OBD, resolution 2.2 Å), has a large highly hydrophobic binding site capable of simultaneously binding up to four lipid molecules [4]. In human plasma, CETP plays a potentially proatherogenic role by moving CE from HDL to very-low-density lipoprotein (VLDL) and low-density lipoprotein (LDL) particles, thereby lowering atheroprotective HDLc and raising proatherogenic VLDLc and LDLc. Apparently, the risk of CAD is proportional to the plasma levels of CETP [5]. In fact, It is quite common within the CAD population to have elevated CETP plasma protein levels that are 2- to 3-fold higher than concentrations typically found in the plasma of normal subjects (1–3 μg/mL) [6].

Evidence exists that the consequences of CETP activity may depend on the metabolic setting, particularly on triglyceride levels. Accordingly, pharmacological CETP inhibition may reduce the risk of CAD in humans, but only in those with high triglyceride levels [5].

The unavailability of satisfactory high resolution crystallographic structures for CETP combined with its prohibitively large binding pocket confined most modeling-related discovery projects to ligand-based approaches particularly quantitative structure–activity relationship analysis (QSAR) [7–9].

Despite the excellent predictive potential of 3D-QSAR methodologies (e.g., CoMFA and CoMSIA), they generally lack the ability to

Abbreviations: CETP, Cholesteryl ester transfer protein; QSAR, quantitative structure–activity relationship; ROC, receiver-operating characteristic; NCI, national cancer institute; CAD, coronary artery disease; HDLc, high-density lipoprotein cholesterol; CE, cholesteryl esters; LDLc, low-density lipoprotein cholesterol; VLDLc, very-low-density lipoprotein cholesterol; GFA, genetic function algorithm; MLR, multiple linear regression; VS, virtual screening; DAC, drugs and agrochemicals.

* Corresponding author. Tel.: +962 6 5355000x23305; fax: +962 6 5339649.
E-mail address: mutasem@ju.edu.jo (M.O. Taha).

0223-5234/$ – see front matter © 2010 Elsevier Masson SAS. All rights reserved.
doi:10.1016/j.ejmech.2009.12.070

act as effective search queries to mine virtual three-dimensional (3D) databases for new hits [10,11].

The continued interest in the development of new CETP inhibitors combined with the lack of adequate CETP crystallographic structures and adequate computer-aided drug discovery efforts in this area, prompted us to explore the possibility of developing ligand-based three-dimensional (3D) pharmacophore(s) integrated within self-consistent QSAR model for CETP inhibitors. The pharmacophore model(s) can be used as 3D search query(ies) to mine 3D libraries for new CETP inhibitors, while the QSAR model helps to predict the biological activities of the captured compounds and therefore prioritize them for *in vitro* evaluation. We previously reported the use of this innovative approach towards the discovery of new inhibitory leads against glycogen synthase kinase 3β (GSK-3β) [12], dipeptidyl peptidase [13], hormone sensitive lipase (HSL) [14], bacterial MurF [15], protein tyrosine phosphatase 1B (PTP 1B) [16] and influenza neuraminidase [17].

We employed the HYPOGEN module from the CATALYST software package to construct numerous plausible binding hypotheses for CETP inhibitors [18]. Subsequently, genetic function algorithm (GFA) and multiple linear regression (MLR) analysis were employed to search for an optimal QSAR that combines high-quality binding pharmacophores with other molecular descriptors and capable of explaining bioactivity variation across a collection of diverse CETP inhibitors. The optimal pharmacophores were further validated by evaluating their ability to successfully classify a list of compounds as actives or inactives by assessing their receiver-operating characteristic (ROC) curves. Subsequently, the optimal pharmacophores were complemented with tight shape constraints to enhance their ROC profiles. Thereafter, the resulting shape-complemented pharmacophores were used as 3D search queries to screen several available virtual molecular databases for new CETP inhibitors. Active hits were employed as guides to synthesize new series of active CETP inhibitors.

CATALYST models drug–receptor interactions using information derived from the ligand structures [18–26]. HYPOGEN identifies a 3D array of a maximum of five chemical features common to active training ligands that provides relative alignment for each input molecule consistent with binding to a proposed common receptor site. The conformational flexibility of training ligands is modeled by creating multiple conformers that cover a specified energy range for each input molecule [16,21–23,27–31].

The SHAPE module in CATALYST is a shape-based similarity searching method. The Van der Waals surface of a molecule (in a certain conformation) is calculated and represented as a set of points of uniform average density on a grid. The surface points enclose a volume on the grid. The geometric center of the set of points is computed along with the three principal component vectors passing through the center. The maximum extents along each principal axis and the total volume are calculated. These provide shape indices that can be compared with the query and used in an initial screening step to eliminate poor matches from further consideration [32]. CATALYST pharmacophores, with or without shape constraints, have been used as 3D queries for database searching and in 3D-QSAR studies [21,23,27,32].

2. Results and discussion

2.1. Pharmacophore modeling

The literature was extensively surveyed to collect diverse CETP inhibitors. A dataset of 118 *N,N*-disubstituted-3-amino-2-propanol derivatives (**1–118**, Table A under Supplementary material) was used for pharmacophore modeling and subsequent QSAR analysis [33–36]. The conformational space of each inhibitor was sampled utilizing the poling algorithm implemented within CATALYST [21–23,37].

The pharmacophoric space of CETP inhibitors was explored employing three structurally diverse training subsets of inhibitors (Table 1). The pharmacophoric space of each training subset was explored *via* four HYPOGEN runs (Table B under Supplementary material). We restricted HYPOGEN to explore pharmacophoric models incorporating from zero to three features of any particular selected feature type (i.e., HBA, HBD, hydrophobic and Ring Aromatic) to limit the number of explored pharmacophoric models and therefore improve the quality of emerging binding hypotheses [12–17]. Only four and five-featured pharmacophores were explored. Three- and two-featured pharmacophores are rather promiscuous as 3D search queries and probably not adequate descriptions of ligand-CETP binding as judged from the structural diversity of the training compounds. CATALYST–HYPOGEN can generate pharmacophore hypotheses of a maximum of five features [22,23].

We allowed a maximum of 4–5 features per pharmacophore in runs 1 and 2; however, runs 3 and 4 were limited to five-featured pharmacophores only. The same trend is followed with other training subsets (i.e., sets II and III). Despite bias towards five-featured hypotheses in this conduct, differences in the ranges of allowed pharmacophoric features should force CATALYST to explore different sections of the pharmacophoric space of CETP inhibitors. This assumption is supported by significant differences in the success profiles of resultant pharmacophore models, i.e., cost criteria, particularly config. costs (Table C under Supplementary material). Similarly, to explore the optimal pharmacophoric inter-feature distances, we evaluated two inter-feature spacing values: 100 and 300 pm (as in Table B under Supplementary material).

Eventually, 10 optimal pharmacophoric hypotheses were generated for each run, yielding 40 models for each set of inhibitors, i.e., 120 models from the three training subsets. Table C, under Supplementary material, shows the pharmacophoric features and success criteria of best-performing representative pharmacophores [26,38]. The resulting pharmacophore models shared comparable features and acceptable statistical criteria. Emergence of several comparable binding hypotheses suggests the existence of multiple binding modes assumed by different CETP ligands within the binding pocket.

2.2. QSAR modeling

Despite the significance of pharmacophoric hypotheses in understanding ligand-macromolecule affinity and as 3D search queries, their predictive value as 3D-QSAR models is generally limited by steric shielding and bioactivity-modulating auxiliary groups (electron-donating or electron-withdrawing functionalities) [12–17,25]. This point combined with the fact that our pharmacophore exploration of CETP inhibitors identified numerous successful binding hypotheses (as in Table C under Supplementary material) prompted us to employ classical QSAR analysis to search for the best combination of orthogonal pharmacophores and other structural descriptors (connectivity, topological, 2D, etc.) capable of explaining bioactivity variation across the whole training list

Table 1
Training subsets employed in exploring the pharmacophoric space of CETP inhibitors, numbers correspond to compounds in Table A (under Supplementary material).

Training set	Most active subset[a]	Intermediate subset	Least active subset[a]
I	**1, 2, 4, 7, 21**	**23, 42, 43, 44, 53, 59, 67, 76, 80, 88, 114**	**92, 93, 96, 97**
II	**1, 4, 102, 104, 105, 106**	**7, 29, 42, 53, 58, 76, 110, 111**	**86, 88, 89, 93, 96, 97, 112, 113**
III	**3, 8, 10, 11, 16, 17, 21, 23**	**36, 50, 54, 67, 68, 80, 83, 89**	**93, 94, 95, 96, 97, 99**

[a] Potency categories as defined by Eqs. (2) and (3).

(**1–118**, Table A under Supplementary material). Eq. (1) shows our best-performing QSAR model. Fig. 1 shows the corresponding scatter plots of experimental versus estimated bioactivities for the training and inhibitors.

$$\log(1/IC_{50}) = -1.642 + 0.186\ \text{Hypo 12/4} + 0.351[\text{Hypo 4/8} - 4.98] - 0.032[\text{ShadowXZ} - 70.306] - 0.184[\text{AtypeH47} - 18.00] - 0.147\ \text{SaaN}$$

$$r^2_{96} = 0.800,\ F = 72.1,\ n = 96,\ r^2_{BS} = 0.800,\ r^2_{LOO} = 0.775,\ r^2_{PRESS} = 0.707 \quad (1)$$

where, r^2_{96} is the correlation coefficient, F is Fisher statistical parameter, n is the number of observations, r^2_{BS} is the bootstrapping regression coefficient, r^2_{LOO} is the leave-one-out correlation coefficient and r^2_{PRESS} is the predictive r^2 determined for 22 randomly selected external test compounds [39–43]. Shadow-XZ is the area of the molecular shadow in the XZ plane. It is a geometric descriptor that characterizes the shape of the molecule and depends on molecular conformation and orientation. AtypeH47 is atom-type-based AlogP descriptor. SaaN is the electro-topological sum descriptor (E-state descriptor). E-state descriptors encode information about both the topological environment of the particular atom and the electronic interactions due to all other atoms in the molecule. SaaN is the sum of E-State values of all nitrogen atoms with two aromatic bonds found in the molecule [40,44]. Hypo4/8 and Hypo12/4 represent the fit values of the training compounds against the 8th and 4th pharmacophores generated in the 4th and 12th modeling runs, respectively (Tables B and C under Supplementary material) [40].

The excellent qualities of Eq. (1) are evident not only from its excellent statistical criteria, i.e., r^2, F, r^2_{BS}, r^2_{LOO}, r^2_{PRESS}, but also from the orthogonality of its descriptor variables (see Table 2).

Several descriptors emerged in Eq. (1) in spline format, e.g., Hypo4/8. The spline terms employed herein are "truncated power splines" and are denoted by bolded brackets (**[ ]**). For example, **[**$f(x) - a$**]** equals zero if the value of $(f(x) - a)$ is negative; otherwise, it equals $(f(x) - a)$ [40].

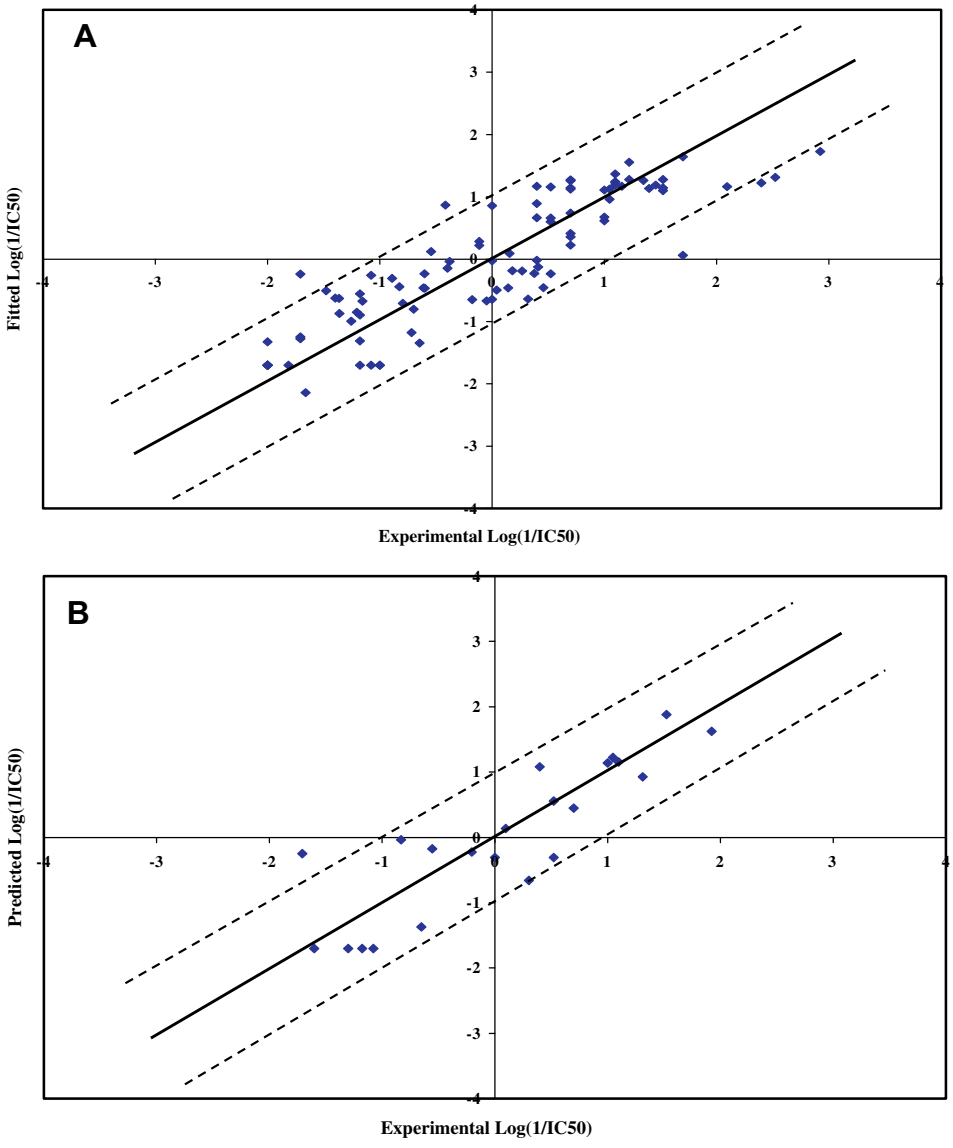

Fig. 1. Experimental versus fitted (A, 96 compounds, $r^2_{LOO} = 0.775$) and predicted (B, 22 compounds, $r^2_{PRESS} = 0.707$) bioactivities calculated from the best QSAR model (Eq. (1)). The solid lines are the regression lines for the fitted and predicted bioactivities of training and test compounds, respectively, whereas the dotted lines indicate the 1.0 log point error margins.

Table 2
Cross-correlation coefficients (r^2) of different descriptors in QSAR Eq. (1).[a]

	Hypo12/4	AtypeH47	Shadow-XZ	SaaN
AtypeH47	0.09			
Shadow-XZ	0.20	0.19		
SaaN	0.01	0.03	0.04	
Hypo4/8	0.57	0.04	0.28	0.00

[a] Correlation coefficients were determined against compounds **1**–**118** (Table A in Supplementary material).

Interestingly, the combination Hypo4/8 and Hypo12/4 frequented in the highest-ranking QSAR equations suggesting they represent two complementary binding modes accessible to ligands within the binding pocket of CETP, i.e., one of them can optimally explain the bioactivities of some training inhibitors, while other inhibitors are more appropriately explained by the second pharmacophore [28]. Fig. 2 shows the two pharmacophores and how they map to the most potent inhibitor **100** ($IC_{50} = 0.0012$ μM), while Table D, under Supplementary material, shows the *X*, *Y*, and *Z* coordinates, weights and tolerances of their pharmacophoric features.

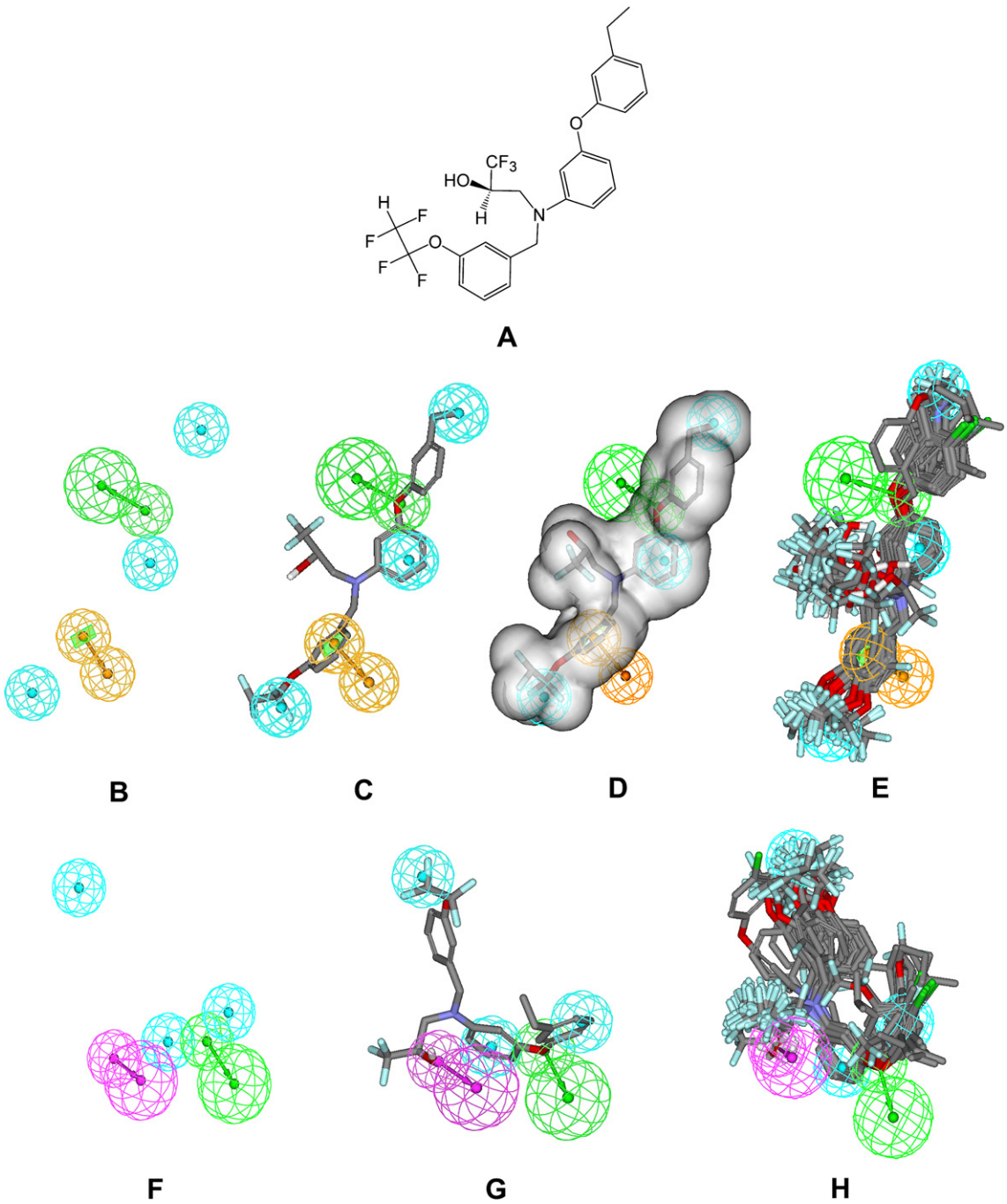

Fig. 2. The binding pharmacophore hypotheses emerging in the optimal QSAR model (Hydrogen bond acceptor as green vectored spheres, hydrophobic features as blue spheres, ring aromatic as orange vectored spheres, Hydrogen bond donor as violet vectored spheres): (A) the most potent inhibitor **100** (Table A under Supplementary material, $IC_{50} = 0.0012$ μM), (B) Hypo4/8, (C) Hypo4/8 mapped against **100**, (D) shape-complemented Hypo4/8 mapped against **100**, (E) Hypo4/8 mapped against most potent 30 training compounds, (F) Hypo12/4, (G) Hypo12/4 mapped against **100**, and (H) Hypo12/4 mapped against most potent 30 training compounds. (For interpretation of the references to colour in this figure legend, the reader is referred to the web version of this article.)

Intriguingly, Hypo4/8 emerged in Eq. (1) in spline format indicating that this binding mode contributes to ligand/CETP affinity only if it fits a particular ligand above the corresponding spline threshold. Accordingly, the ability of certain ligand to fit Hypo4/8 will impact its actual affinity to CETP only if its fit value exceeds 4.98 (the spline intercept associated with this pharmacophore in Eq. (1)). Since this spline cutoff resembles moderate ligand/pharmacophore mapping, as the maximum fit value is 12.0, it appears that ligand binding to CETP is sensitive to moderate misalignments among the attracting moieties within the complex, such that lowering the fit value below 4.98 nullifies any affinity gains from mapping this pharmacophore.

Emergence Shadow descriptors (i.e., shadow-xz) in Eq. (1) illustrates certain role played by the ligands' topology in the binding process. However, despite their predictive significance, the information content of such descriptors is quite obscure [44]. Nevertheless, emergence of SaaN in combination with a negative regression slope suggests that the presence of nitrogen-containing heterocycles reduces anti-CETP activity, as seen in compounds **57**, **66**, **70**, **71**, **79**, **81**, and **87** (Table A under Supplementary material). This conduct might be related to certain aromatic π-stacking interactions involving the ligands and certain electron-deficient center(s) in the binding pocket such that the switching electron-rich aromatic rings with electron-deficient nitrogen heterocycles within the ligand structures disrupts this interaction causing the apparent reduction in activity.

On the other hand, emergence of AtypeH47, which encodes for the hydrophobic contribution of hydrogen atoms [40], in association with a negative slope, suggests that the binding pocket favors hydrophilic ligands as it seems to occur at the hydrophilic outer surface of CETP.

2.3. Receiver-operating characteristic (ROC) curve analysis and shape constraints

To further validate the resulting models (both QSAR and pharmacophores), we subjected our QSAR-selected pharmacophores to receiver-operating curve (ROC) analysis (see Section 4.3 for more details).

Table 3 and Fig. 3 show the ROC results of our QSAR-selected pharmacophores. Hypo4/8 illustrated mediocre overall performance with an AUC of 71.95%. On the other hand, Hypo12/4 exhibited excellent performance with AUC value of 99.91%. This is not unexpected, as the presence of HBA and HBD features in Hypo12/4 points to its hydrophilic nature and therefore its better selectivity. While on the other hand, the hydrophobic nature of Hypo4/8 might explain its observed inferior selectivity. Well-positioned hydrophilic groups should promote selective ligand-receptor interactions and accordingly promote pharmacophoric selectivity and ROC-AUC [45].

In order to enhance the ROC profile of Hypo4/8, we decided to decorate it with shape constraints derived from the most potent training inhibitor **100** ($IC_{50} = 0.0012$ μM). Shape constraints encode for the degree of 3D spatial similarity between screened compounds and the template ligand used to build the shape limitations [18]. We employed the most potent training compound **100** ($IC_{50} = 0.0012$ μM) as shape template (see Section 4.4 for more details).

Fig. 3 and Table 3 show the ROC result of the shape-decorated version of Hypo4/8. Clearly, the performance of shape-complemented Hypo4/8 improved significantly as reflected by its ROC-AUC, which shifted from 71.95% to 94.20%.

Table 3
Performance of QSAR-selected pharmacophores and the shape-complemented version of Hypo4/8 as 3D search queries.

Pharmacophore model	ROC–AUC	ACC	SPC	TPR	FNR
Hypo4/8	0.7195	0.9522	0.9532	0.9333	0.0468
Hypo12/4	0.9991	0.9522	0.9498	1.0000	0.0502
Shape-complemented Hypo4/8	0.9420	0.9522	0.9565	0.8667	0.0435

ROC, receiver-operating characteristic; AUC, area under the curve; ACC, overall accuracy; SPC, overall specificity; TPR, overall true positive rate; FNR, overall false negative rate.

2.4. In silico screening of databases

Despite its less-than-optimal ROC profile, we were prompted by group of factors to employ Hypo4/8 as the primary 3D search query against available 3D structural databases. These factors can be summarized as follows: (i) Hypo4/8 frequented in high-ranking QSAR models significantly more than Hypo12/4, (ii) Hypo4/8 was associated with higher regression coefficient in the optimal QSAR Eq. (1) compared to Hypo12/4 and (iii) the term **[**Hypo4/8 − 4.98**],** in Eq. (1), is statisitcally more significantly connected to bioactivity (i.e., $Log(1/IC_{50})$) compared to Hypo12/4 with coresponding significance *F*-values of 134.0 and 42.0, respectively.

However, to improve the success rate of our virtual screening, we decided to refine Hypo4/8 search hits by either: (A) subsequent screening of the hit list by Hypo12/4 (select hits captured by both Hypo4/8 and Hypo12/4), or (B) shape constraints implemented on Hypo4/8 (Fig. 2D).

In silico screening was conducted against the national cancer institute list of compounds (NCI, includes 238,819 compounds) [18] as well as our *in house* built list of drugs and agrochemicals (DAC, 3002 compounds). NCI hits were subsequently filtered by Lipinski's [46] and Veber's criteria [47]. However, DAC hits were left without subsequent filtration. Table 4 shows the number captured hits by both methods, i.e, sequential pharmacophore refinement or shape constraints.

Surviving hits were fitted against Hypo4/8 and Hypo12/4 (fit values determined by Eq. (5) in Section 4) and their fit values were substituted in QSAR Eq. (1) to determine their predicted bioactivities. However, in order to minimize the impact of any possible extrapolatory QSAR prediction errors on decisions regarding which hits merit subsequent *in vitro* testing [10,41], we employed Log $(1/IC_{50})$ predictions merely to rank the corresponding hits and prioritize subsequent *in vitro* testing [12–17]. Table 5 and Fig. 4 show the highest predicted hits, their QSAR-based predictions, as well as their experimental *in vitro* bioactivities.

Out of the 52 highest-ranking hits acquired for experimental validation, 25 were found to possess inhibitory activities against CETP ranging from 5.7 to 82.5% at 10 μM. Four hits, namely, **120** (NSC 40331), **130** (Glypuride), **141** (NSC 186323) and **162** (NSC 89508) exhibited >30% CETP inhibition at 10 μM prompting us to evaluate their IC_{50} values. Fig. 5 shows how Hypo4/8 and Hypo12/4 fits **120** ($IC_{50} = 6.5$ μM), while Fig. 6 shows how shape-complemented Hypo4/8 maps **162** ($IC_{50} = 1.9$ μM).

Interestingly, although the sequential search method achieved higher percentage of active hits (23 actives from 43 captured) compared to shape-constrained Hypo4/8 (2 actives from 9 hits), the later method captured the most potent hit (**162**) with IC_{50} value of 1.9 μM. The capture of a majority of inactive hits by shape-complemented Hypo4/8 is probably due to factors related to favorable hydration (**163** and **164**, Fig. 4) or excessive structural rigidity (**165**–**170**, Fig. 4).

Although Eq. (1) failed to identify inactive search hits, it predicted the bioactivities of active hits excellently, as evident in Table 5. In fact, it predicted the IC_{50} values of **120**, **130**, **141** and **162** to be 7.9, 794.3, 33.0 and 0.9 μM, respectively, which agrees nicely with the experimental values 6.5, 238.6, 60.3 and 1.9 μM, respectively. This conduct is probably due to the lack of structural diversity in

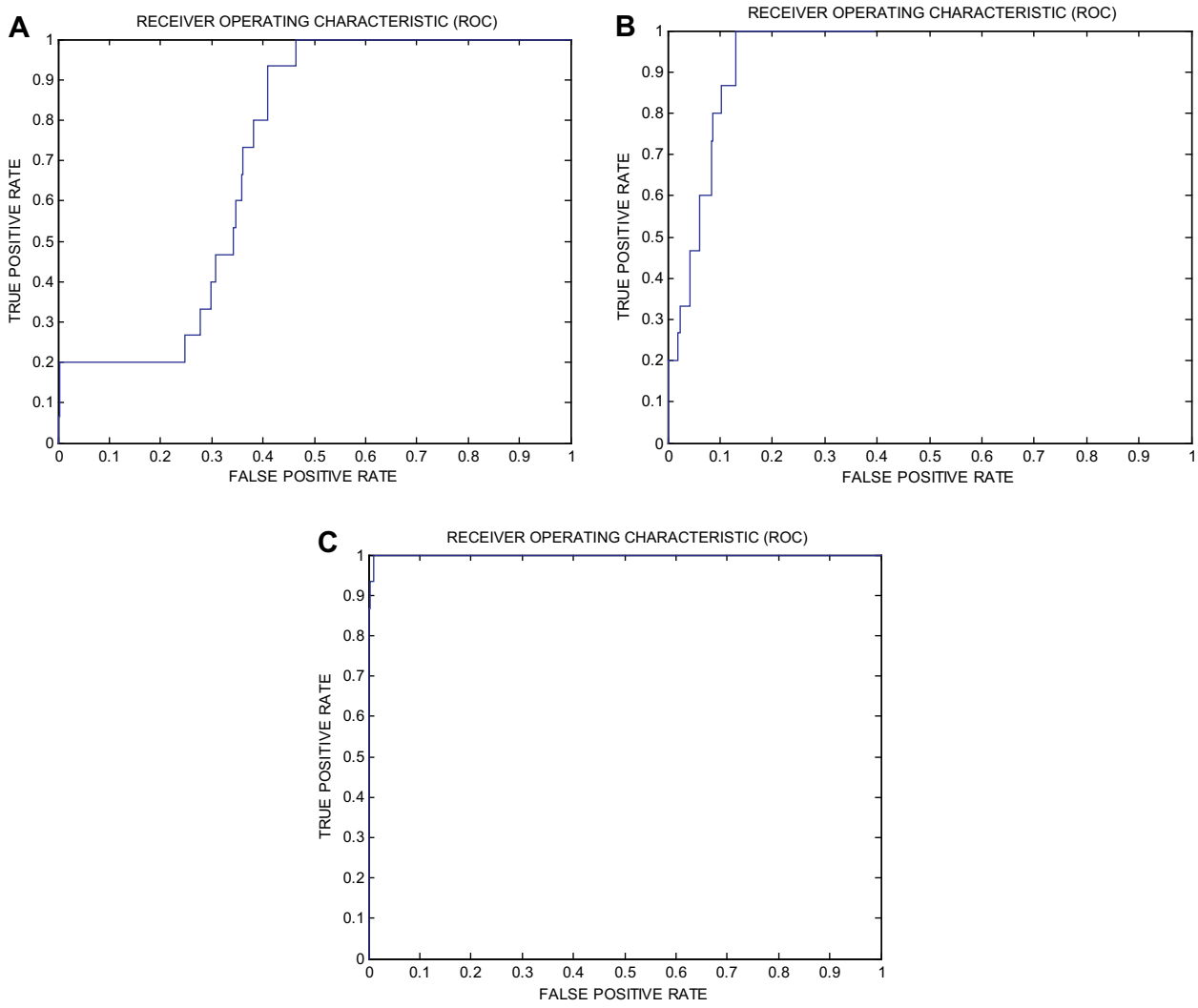

Fig. 3. Receiver operating characteristic curves (ROCs) of (A) Hypo4/8, (B) shape-complemented Hypo4/8, (C) and Hypo12/4.

our training list of compounds thus restricting the extrapolatory potential of resulting QSAR models to limited structural categories.

2.5. Synthesis and scaffold exploration

Convergence of *in silico* modeling studies and subsequent *in vitro* validation on CETP inhibitors based on three-aromatic ring scaffold interrupted with hydrogen-bond acceptor feature, e.g., **120** and **162** (see Figs. 5 and 6), prompted us to envisage a new class of inhibitors that enclose at least three aromatic rings. Moreover, we hypothesized that introducing two well-positioned central HBA features within the scaffold should maximize ligand-CETP binding by allowing the ligands to tightly map Hypo4/8 in at least two poses. In this context, we prepared 11 new benzylidene-amino methanones containing two opposing HBAs: imine and ketone.

Schemes 3 and 4 show the new structures (**187**–**190** and **193**–**199**) while Fig. 7 shows how Hypo4/8 maps compounds **189** and **190**. The HBA of Hypo4/8 fits the imine of **189** and ketone of **190** as anticipated.

The synthesis commenced by preparing different substituted aminobenzophenone intermediates (**175**–**177** and **180**–**182**), in modest to reasonable yields, *via* Friedel–Crafts acylation of benzene and substituted derivatives (**172**–**174** and **179**) with 3- and 4-aminobenzoic acids (**171** and **178**) in the presence of polyphosphoric acid (PPA) [48] as in Schemes 1 and 2.

The best yield was obtained upon reacting 4-aminobenzoic acid with 1,3-dimethoxybenzene to yield **182** (89%). Unsurprisingly, benzenes substituted with electron-donating groups afforded good yields, while electron-deficient benzene rings and biphenyl required higher reaction temperatures and gave products with low yields.

Table 4
The number of captured hit compounds by search methods.

3D Database[a]	Post-screening filtering[b]	Search method	
		Sequential Hypo4/8 followed by Hypo12/4	Shape-complemented Hypo4/8
NCI	Before	5205	1232
	After	516	527
DAC[c]	None	121	55

[a] NCI: national cancer institute list of available compounds (238,819 structures), DAC: the list of established drugs and agrochemicals (3002 structures).
[b] Post-screening filtering employing Lipinski's and Veber's rules.
[c] This list of compounds was *in silico* scanned without post-screening filtering.

Table 5
The captured hit molecules with their fit values, their corresponding QSAR estimates from Eq. (1) and their *in vitro* bioactivities.

Tested hits[a]	Search method[b]	Fit values against[c]				*In vitro* Anti-CETP activity	
		Hypo4/8	Hypo12/4	QSAR-based estimates		% Inhibition at 10.0 μM	IC_{50} (μM)
				$Log(1/IC_{50})$	IC_{50} (μM)		
119	A	2.6	7.3	−1.9	79.4	12.3	–
120	A	7.8	2.2	−0.9	7.9	52.5	6.5 (0.99)[d]
121	A	6.7	2.3	−0.7	5.0	22.1	–
122	A	2.8	3.9	−1.8	63.1	18.6	–
123	A	8.3	1.2	−2.7	501.2	20.8	–
124	A	7.7	6.4	−0.5	3.2	0.0	–
125	A	6.2	4.4	−1.8	63.1	10.6	–
126	A	5.2	5.0	−1.8	63.1	0.0	–
127	A	2.3	1.7	−2.1	125.9	0.0	–
128	A	5.6	3.3	−1.2	15.8	0.0	–
129	A	7.5	6.0	−1.3	20.0	5.7	–
130	A	3.2	0.0	−2.9	794.3	35.0	238.6 (1.00)[d]
131	A	7.1	7.4	−0.8	6.3	15.9	–
132	A	3.2	9.1	−0.2	1.6	11.4	–
133	A	7.0	2.4	−0.9	7.9	0.0	–
134	A	2.3	5.9	−0.9	7.9	0.0	–
135	A	9.0	3.4	0.2	0.6	0.0	–
136	A	4.1	4.0	−1.0	10.0	22.6	–
137	A	1.0	3.3	−1.0	10.0	25.5	–
138	A	8.0	4.9	−0.9	7.9	13.4	–
139	A	9.1	5.4	−0.3	2.0	20.3	–
140	A	8.9	5.9	0.4	0.4	0.0	–
141	A	6.3	3.6	−1.0	10.0	33.0	60.3 (0.99)[d]
142	A	8.6	3.6	−1.0	10.0	0.0	–
143	A	8.5	6.2	0.8	0.2	0.0	–
144	A	9.3	5.7	0.4	0.4	0.0	–
145	A	4.1	6.5	−0.4	2.5	0.0	–
146	A	8.0	7.9	0.0	1.0	0.0	–
147	A	9.1	0.4	−0.9	7.9	9.0	–
148	A	1.9	6.5	−0.5	3.2	14.0	–
149	A	9.7	2.9	0.4	0.4	0.0	–
150	A	1.5	6.2	−0.5	3.2	20.8	–
151	A	2.7	7.8	−0.8	6.3	25.4	–
152	A	4.9	7.1	−0.4	2.5	0.0	–
153	A	3.6	7.4	-0.4	2.5	8.1	–
154	A	7.8	7.5	0.5	0.3	0.0	–
155	A	8.3	7.7	0.8	0.2	9.1	–
156	A	7.8	4.1	−0.6	4.0	0.0	–
157	A	7.0	5.4	−0.1	1.3	6.7	–
158	A	0.0	4.1	−1.0	10.0	0.0	–
159	A	5.5	7.8	−1.0	10.0	27.4	–
160	A	5.1	4.2	−2.0	100.0	0.0	–
161	A	7.6	8.1	0.0	1.0	0.0	–
162	B	9.2	1.2	0.1	0.9	82.5	1.9
163	B	9.2	0.0	−1.2	15.9	6.0	–
164	B	9.3	0.0	−0.4	2.6	0.0	–
165	B	9.5	0.0	−0.3	2.0	0.0	–
166	B	9.7	9.0	0.8	0.1	0.0	–
167	B	9.7	0.0	−0.2	1.4	0.0	–
168	B	9.1	3.0	−0.5	3.2	0.0	–
169	B	9.1	0.0	−0.6	3.8	0.0	–
170	B	9.0	4.0	−0.4	2.2	0.0	–

[a] Compound numbers as in Fig. 4.
[b] A: Sequential search by Hypo4/8 followed by Hypo12/4, B: search by shape-complemented Hypo4/8.
[c] Best-fit values against each binding hypothesis calculated by Eq. (5).
[d] This value represents the correlation coefficient of the corresponding dose-response line at three concentrations.

Subsequently, the aminobenzophenone intermediates were used to prepare the final imines. Imines are formed typically by reversible acid-catalyzed condensation of amines and aldehydes with extrusion of water through either azeotropic distillation or by employing chemical drying agents [49].

In the current work, the imine products were prepared from reaction of benzaldehyde, trifluoro-*m*-tolualdehyde, trifluoro-*p*-tolualdehyde, 3-methoxylbenzaldehyde, 4-methoxylbenzaldehyde and 4-tert-butylbenzaldehyde with aminobenzophenone intermediates (**175**–**177** and **180**–**182**) as illustrated in Schemes 3 and 4 [35]. The best yield was obtained when **176**, dissolved in cyclohexane, reacted with benzaldehyde to yield **187** (70%).

The final products were tested against CETP at 10 μM concentrations and exhibited anti-CETP activities ranging from 9.8 to 33.8% as in Table 6. The less-than-optimal bioactivities of the prepared compounds might be related to their rigid scaffold. We are currently in the process of preparing more flexible analogs of better bioactivity profiles.

3. Conclusions

This work includes elaborate pharmacophore exploration of CETP inhibitors utilizing CATALYST-HYPOGEN. QSAR analysis was employed to select the best combination of molecular descriptors

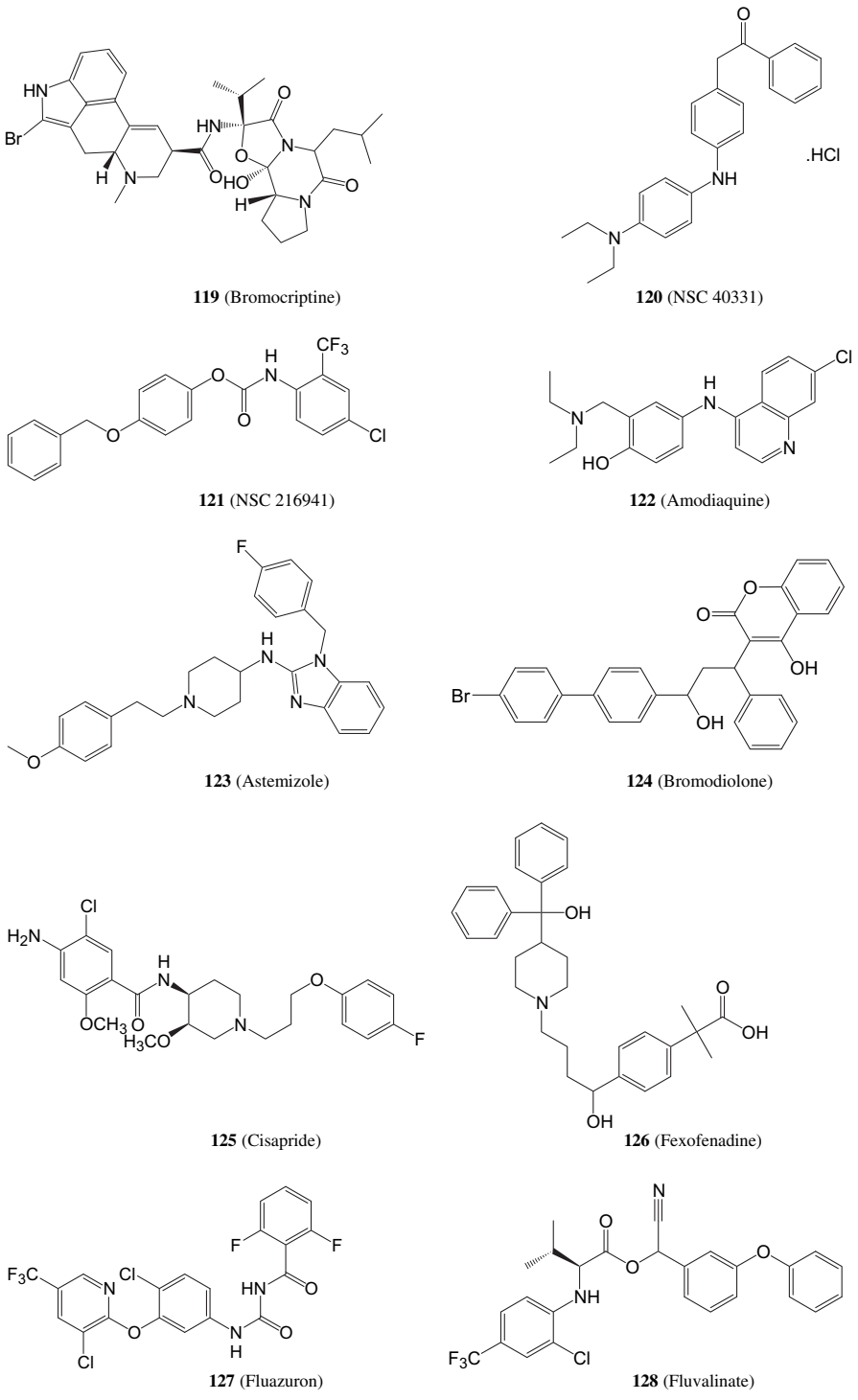

Fig. 4. The chemical structures of the tested highest-ranking hits (as suggested by the best QSAR model and the associated pharmacophores).

and pharmacophore models capable of explaining bioactivity variation across an informative list of training compounds. The successful pharmacophores were complemented with strict shape constraints to optimize their receiver-operating characteristic (ROC) curve profiles. The best binding hypotheses were used as 3D search queries to screen the NCI, drugs and agrochemicals databases for new CETP inhibitors. From the highest-ranking hits, four were found to possess promising inhibitory IC_{50} values against CETP. Modeling results were then used to guide synthetic exploration of a new series of aromatic imines as CETP inhibitors.

4. Experimental section

4.1. Molecular modeling

4.1.1. Software and hardware

The following software packages were utilized in the present research.

- CATALYST (Version 4.11), Accelrys Inc. (www.accelrys.com), USA.

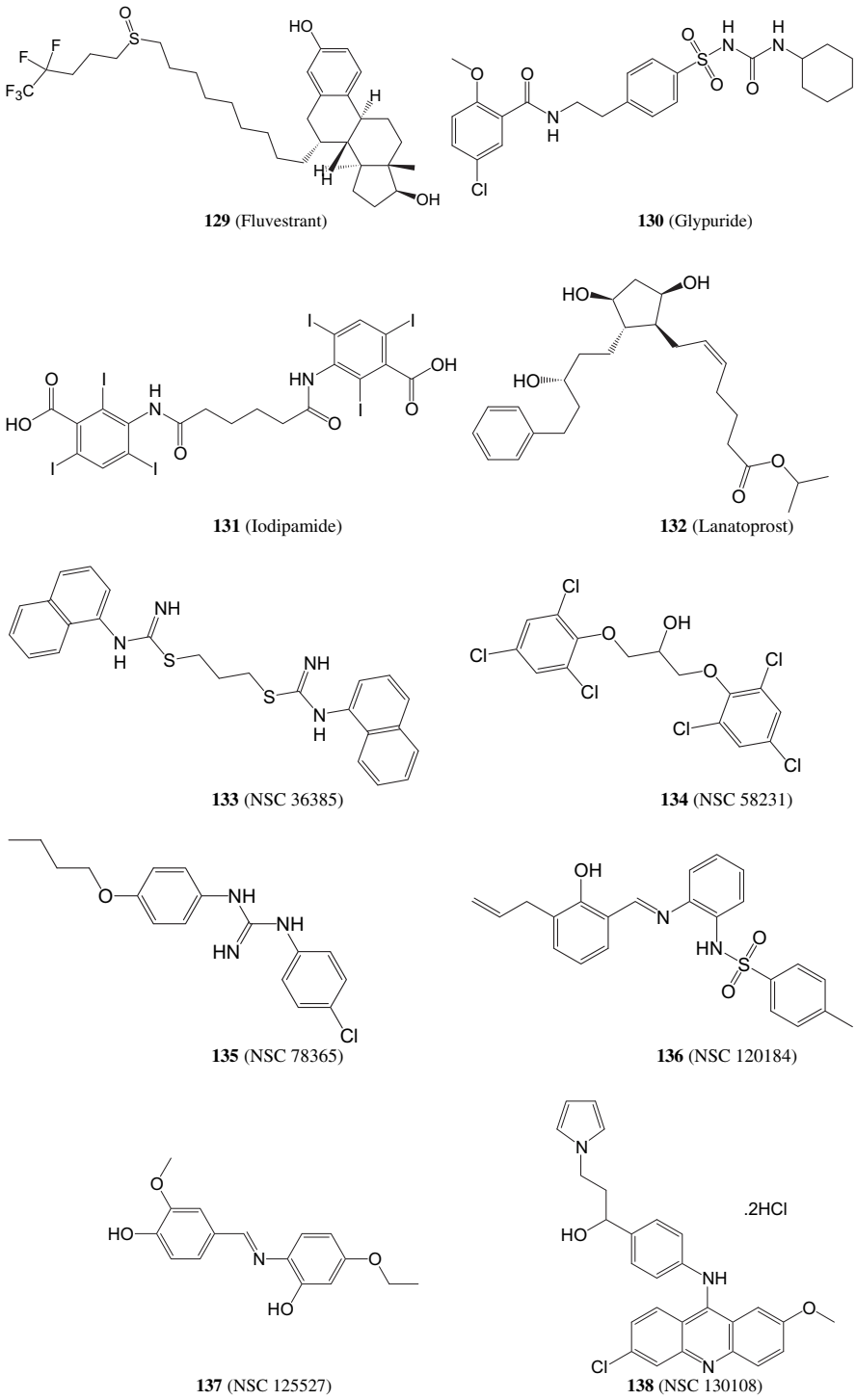

Fig. 4. (*continued*).

- CERIUS2 (Version 4.10), Accelrys Inc. (www.accelrys.com), USA.
- CS ChemDraw Ultra 7.01, Cambridge Soft Corp. (http://www.cambridgesoft.com), USA.

Pharmacophore modeling and QSAR analysis were performed using CATALYST (HYPOGEN module) and CERIUS2 software suites from Accelrys Inc. (San Diego, California, www.accelrys.com) installed on a Silicon Graphics Octane2 desktop workstation equipped with a 600 MHz MIPS R14000 processor (1.0 GB RAM) running the Irix 6.5 operating system.

4.1.2. Dataset

The structures of 118 CETP inhibitors (Table A under Supplementary material) were collected from published literature [33–36]. The *in vitro* bioactivities of the collected inhibitors were expressed as the concentration of the test compound that inhibited the activity of CETP by 50% (IC_{50}). The logarithm of the measured $1/IC_{50}$ values were used in pharmacophore modeling and QSAR analysis, thus correlating the data linear to the free energy change. In cases where IC_{50} is expressed as being higher than 100 μM (e.g., **93, 94, 95, 96, 97, 98** and **99**), we assumed it equals 101 μM. In cases

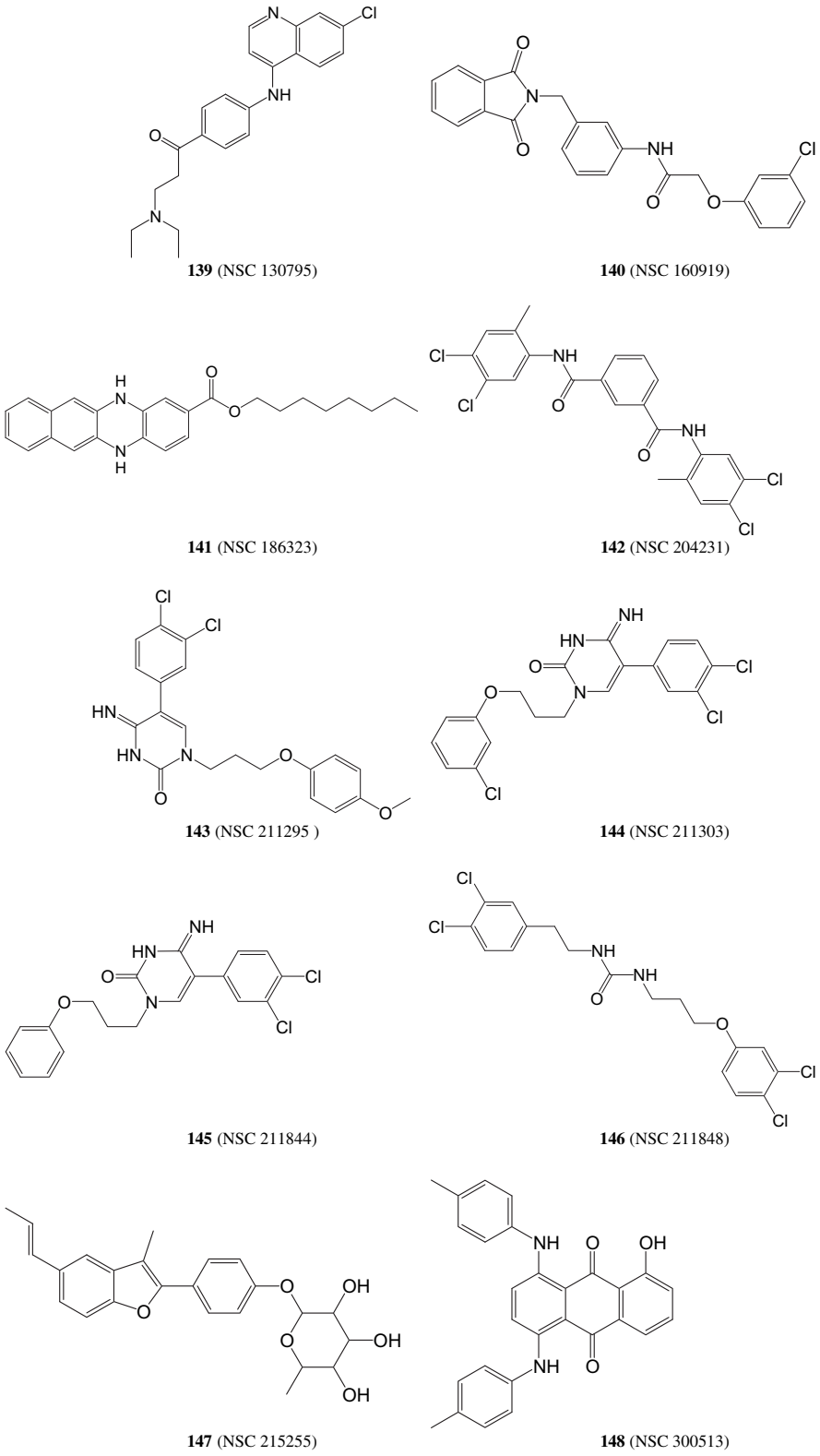

Fig. 4. (*continued*).

where IC_{50} is expressed as being higher than 50 μM (e.g., **91, 116, 117** and **118**), we assumed it equals 51 μM, these assumptions are necessary to allow statistical correlation and QSAR analysis. The logarithmic transformation of IC_{50} values should minimize any potential errors resulting from this assumption.

4.1.3. Conformational analysis

The conformational space of each inhibitor (**1–118**, Table A under Supplementary material) was explored adopting the "best conformer generation" option within CATALYST which is based on the generalized CHARMm force field implemented in the program.

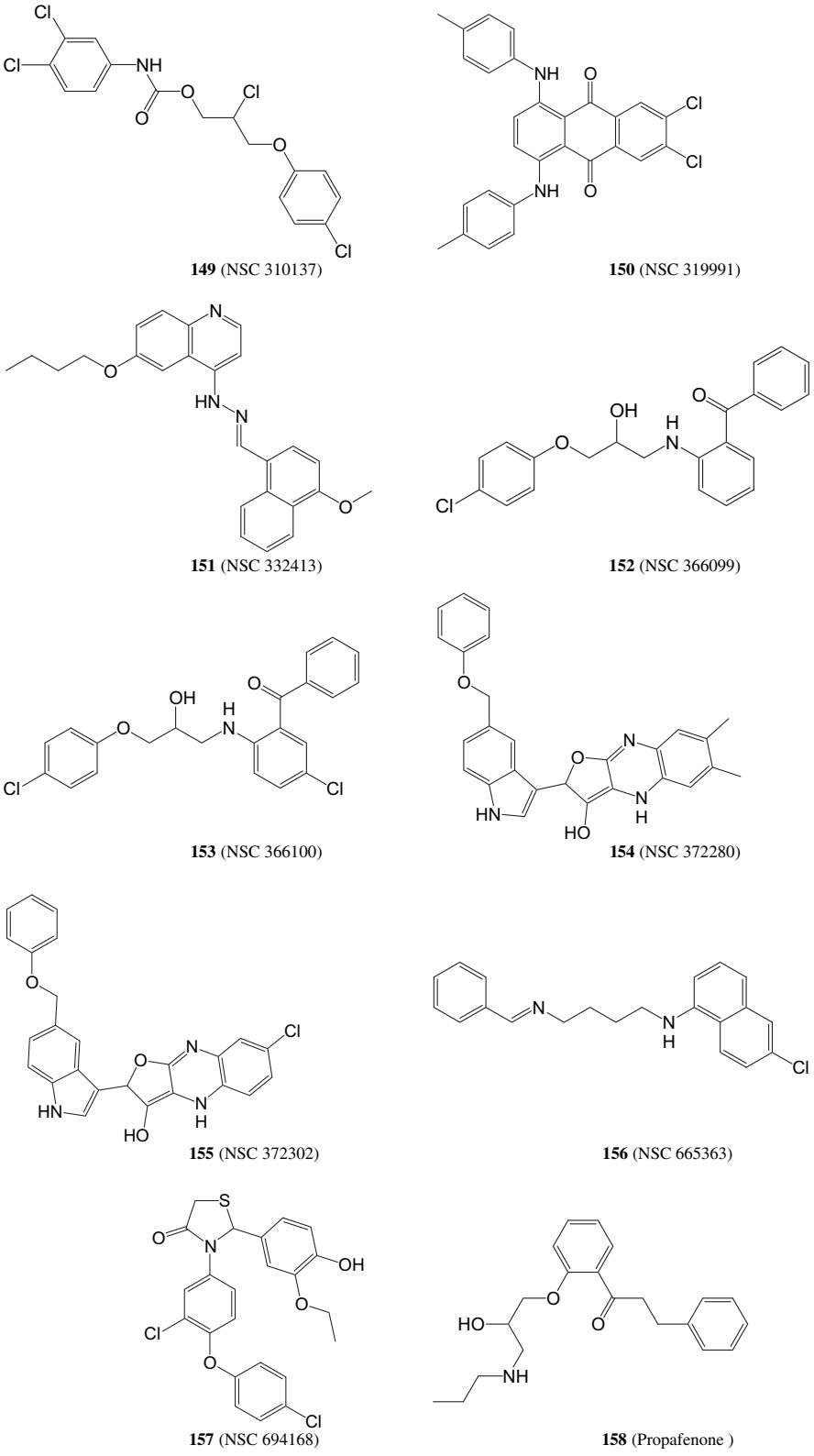

Fig. 4. (*continued*).

Conformational ensembles were generated with an energy threshold of 20 kcal/mol from the local minimized structure and a maximum limit of 250 conformers per molecule [18–20,21–26,37].

4.1.4. Generation of pharmacophoric hypotheses

All 118 molecules with their associated conformational models were regrouped into a spreadsheet. The biological data of the inhibitors were reported with an "Uncertainty" value of 3, which

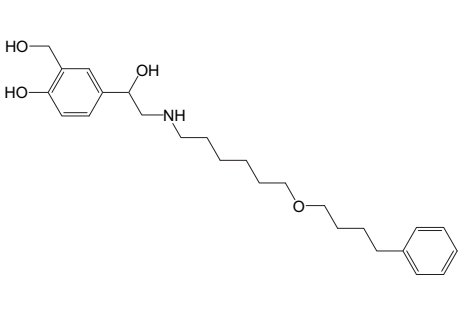

159 (Salmeterol)

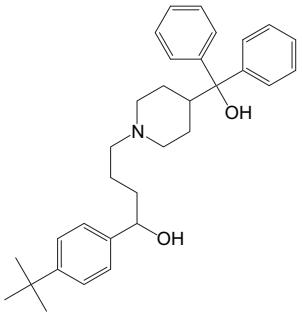

160 (Terfenadine)

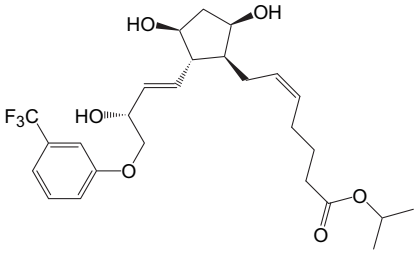

161 (Travoprost)

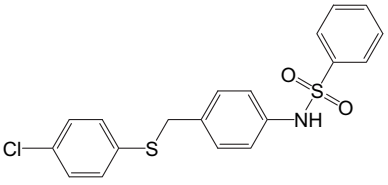

162 (NSC 89508)

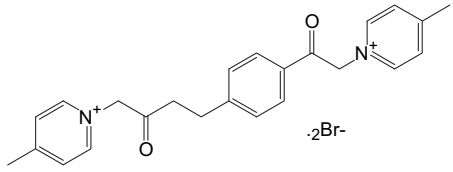

163 (NSC152458)

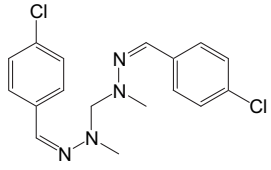

164 (NSC 67226)

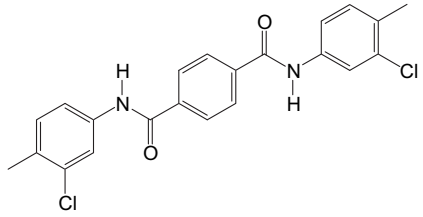

165 (NSC 110302)

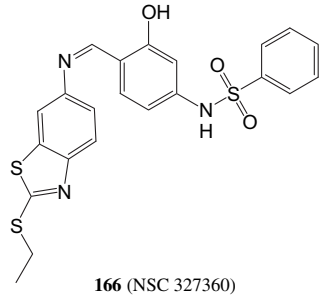

166 (NSC 327360)

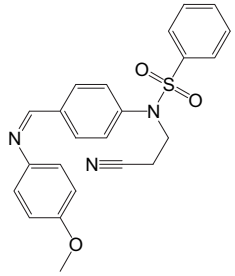

167 (NSC 647954)

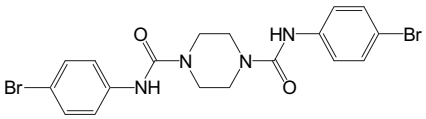

168 (NSC 35927)

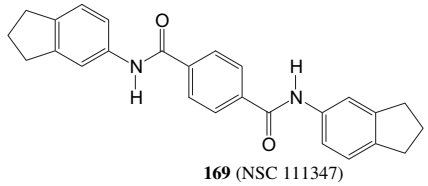

169 (NSC 111347)

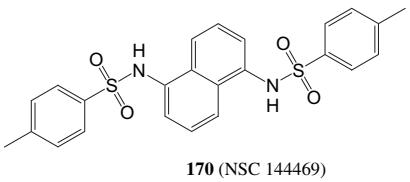

170 (NSC 144469)

Fig. 4. (*continued*).

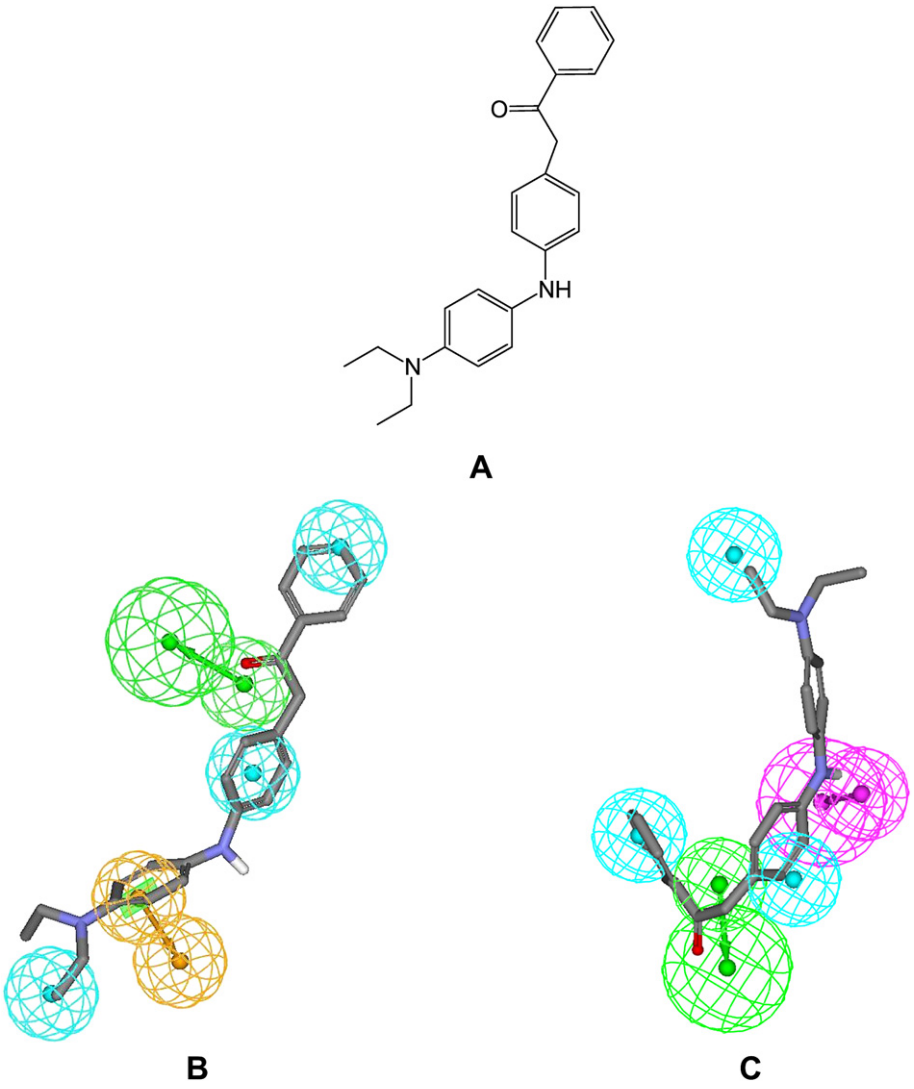

Fig. 5. The mapping of Hypo4/8 and Hypo12/4 against hit **120** (Hydrogen bond acceptor as green vectored spheres, hydrophobic features as blue spheres, ring aromatic as orange vectored spheres, Hydrogen bond donor as violet vectored spheres): (A) inhibitor **120**, (B) Hypo4/8 mapped against **120** and (C) Hypo12/4 mapped against **120.** (For interpretation of the references to colour in this figure legend, the reader is referred to the web version of this article.)

means that the actual bioactivity of a particular inhibitor is assumed to be situated somewhere in an interval ranging from one-third to three-times the reported bioactivity value of that inhibitor [22–26]. Three training subsets (Table 1) were selected for pharmacophore modeling. Each subset was utilized to conduct four modeling runs to explore the pharmacophoric space of CETP inhibitors. Different hypotheses were generated by altering the inter-feature spacing and the number of allowed features in the resulting pharmacophores (Table B under Supplementary material).

Pharmacophore modeling employing CATALYST proceeds through three successive phases: the constructive phase, subtractive phase and optimization phase [22–26]. During the constructive phase, CATALYST generates common conformational alignments among the most active training compounds. Only molecular alignments based on a maximum of five chemical features are considered. The program identifies a particular compound as being within the most active category if it satisfies Eq. (2) [22–26].

$$(\mathrm{MAct} \times \mathrm{UncMAct}) - (\mathrm{Act}/\mathrm{UncAct}) > 0.0 \quad (2)$$

where "MAct" is the activity of the most active compound in the training set, "Unc" is the uncertainty of the compounds and "Act" is the activity of the training compounds under question. In the subsequent subtractive phase, CATALYST eliminates some hypotheses that fit inactive training compounds. A particular training compound is defined as being inactive if it satisfies Eq. (3) [22–26]:

$$\log(\mathrm{Act}) - \log(\mathrm{MAct}) > \mathrm{BS} \quad (3)$$

where, "BS" is the bioactivity spread (equals 3.5 by default).

In the optimization phase, CATALYST applies fine perturbations in the form of vectored feature rotation, adding new feature and/or removing a feature, to selected hypotheses that survived the subtractive phase to find new models of enhanced bioactivity-to-mapping correlations. Eventually, CATALYST selects the highest-ranking models (10 by default) and presents them as the optimal pharmacophore hypotheses resulting from the particular automatic modeling run [19].

4.1.5. Assessment of the generated hypotheses

When generating hypotheses, CATALYST attempts to minimize a cost function consisting of three terms: Weight cost, Error cost and Configuration cost [19,22–26]. Weight cost is a value that increases as the feature weight in a model deviates from an ideal

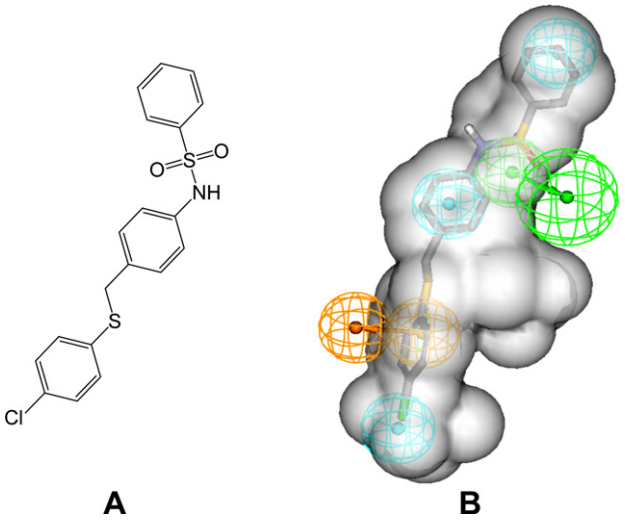

Fig. 6. The mapping of shape-complemented Hypo4/8 pharmacophore hypotheses against hit **162** (Hydrogen bond acceptor as green vectored spheres, hydrophobic features as blue spheres, ring aromatic as orange vectored spheres, Hydrogen bond donor as violet vectored spheres): (A) inhibitor **162** and (B) Hypo4/8 fitted against **162**. (For interpretation of the references to colour in this figure legend, the reader is referred to the web version of this article.)

value of 2. The deviation between the estimated activities of the training set and their experimentally determined values adds to the error cost [19,22–26]. The activity of any compound can be estimated from a particular hypothesis through Eq. (4) [19].

$$\log(\text{Estimated activity}) = I + \text{Fit} \tag{4}$$

where, I = the intercept of the regression line obtained by plotting the log of the biological activity of the training set compounds against the Fit values of the training compounds. The Fit value for any compound is obtained automatically employing Eq. (5) [22–24].

$$\text{Fit} = \sum \text{mapped hypothesis features} \times W\left[1 - \sum (\text{disp/tol})^2\right] \tag{5}$$

where, Σ mapped hypothesis features represents the number of pharmacophore features that successfully superimpose (i.e., map or overlap with) corresponding chemical moieties within the fitted compound, W is the weight of the corresponding hypothesis feature spheres. This value is fixed to 1.0 in CATALYST-generated models. disp is the distance between the center of a particular pharmacophoric sphere (feature centroid) and the center of the corresponding superimposed chemical moiety of the fitted compound; tol is the radius of the pharmacophoric feature sphere (known as Tolerance,

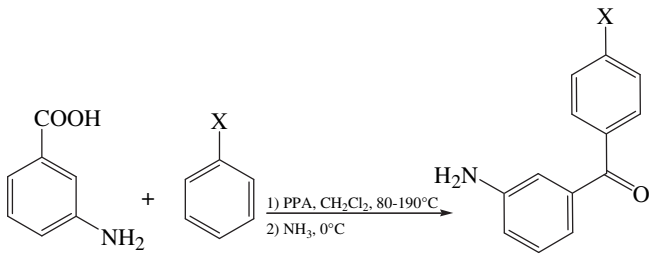

171

172 X = H
173 X = OCH_3
174 X = Phenyl

175 X = H
176 X = OCH_3
177 X = Phenyl

Scheme 1. Synthesis of aminobenzophenone intermediates **175–177**.

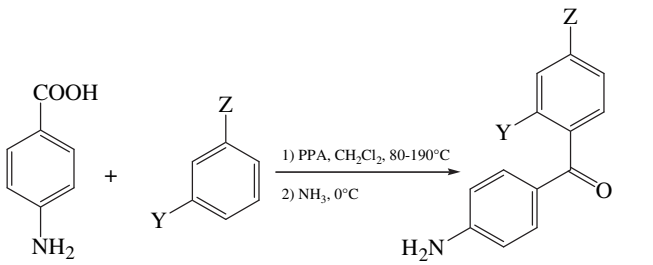

178

172 Y = H, Z = H
174 Y = H, Z = Phenyl
179 Y = OCH_3, Z = OCH_3

180 Y = H, Z = H
181 Y = H, Z = Phenyl
182 Y = OCH_3, Z = OCH_3

Scheme 2. Synthesis of aminobenzophenone intermediates **180–182.**

equals to 1.6 Å by default). $\Sigma(\text{disp/tol})^2$ is the summation of $(\text{disp/tol})^2$ values for all pharmacophoric features that successfully superimpose corresponding chemical functionalities in the fitted compound [22–24].

The third term, i.e., the configuration cost, penalizes the complexity of the hypothesis, i.e. the configuration cost. This is a fixed cost, which is equal to the entropy of the hypothesis space. The more the numbers of features (a maximum of five) in

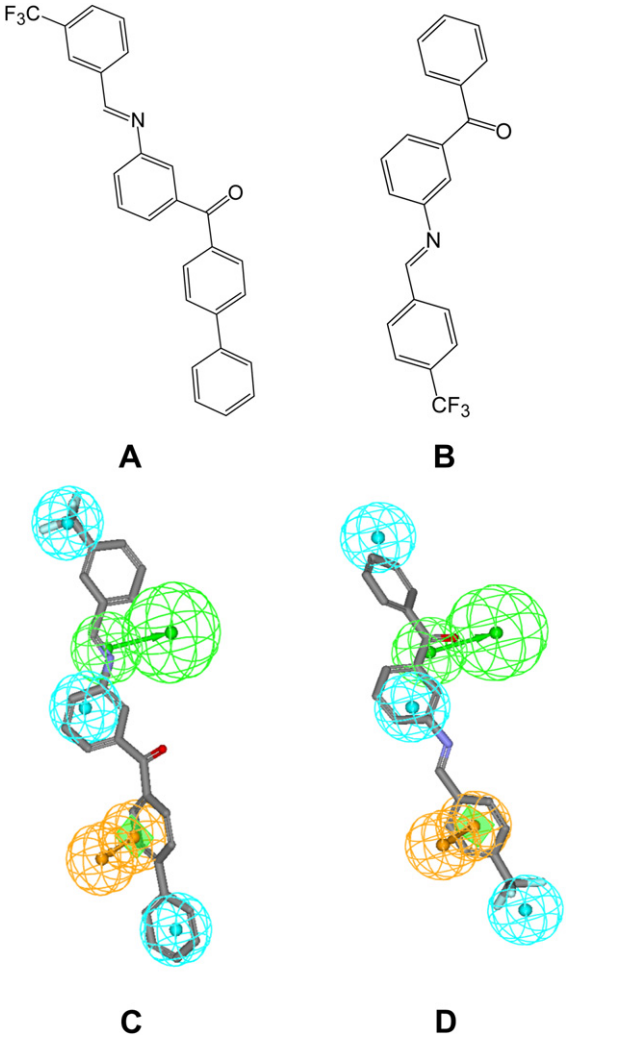

Fig. 7. The mapping of Hypo 4/8 against synthesized compounds **189** (CETP inhibition at 10 μM = 33.8%) and **190** (CETP inhibition at 10 μM = 26.3%): (A) structure of **189**, (B) structure of **190**, (C) Hypo4/8 mapped against **189** and (D) Hypo4/8 mapped against **190**.

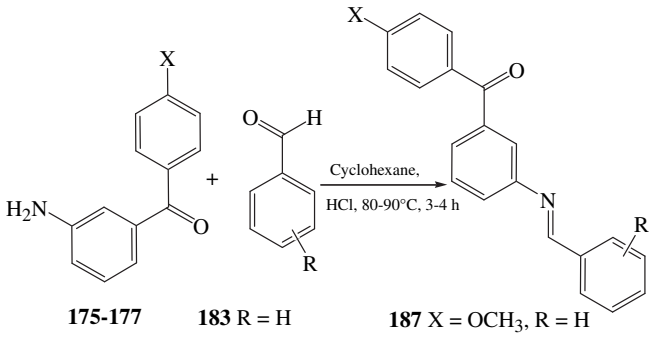

175-177

183 R = H
184 R = 4-OCH_3
185 R = 3-CF_3
186 R = 4-CF_3

187 X = OCH_3, R = H
188 X = OCH_3, R = 4-OCH_3
189 X = Phenyl, R = 3-CF_3
190 X = H, R = 4-CF_3

Scheme 3. Synthesis of imine compounds **187–190**.

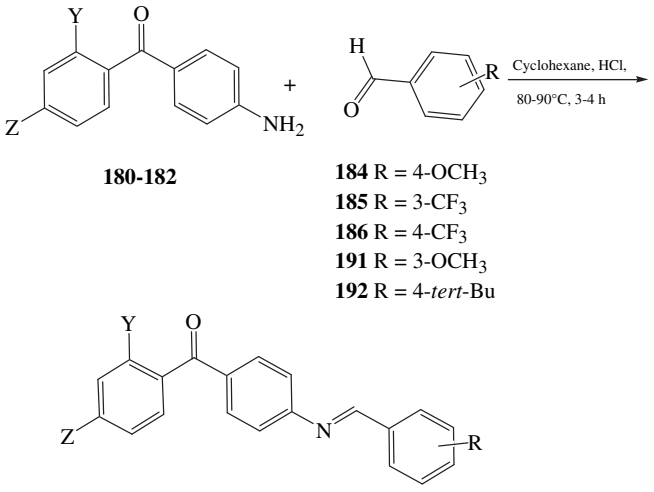

180-182

184 R = 4-OCH_3
185 R = 3-CF_3
186 R = 4-CF_3
191 R = 3-OCH_3
192 R = 4-*tert*-Bu

193 Y = H, Z = Phenyl, R = 3-CF_3
194 Y = OCH_3, Z = OCH_3, R = 4-*tert*-Bu
195 Y = OCH_3, Z = OCH_3, R = 4-CF_3
196 Y = OCH_3, Z = OCH_3, R = 3-CF_3
197 Y = OCH_3, Z = OCH_3, R = 4-OCH_3
198 Y = OCH_3, Z = OCH_3, R = 3-OCH_3
199 Y = H, Z = H, R = 4-OCH_3

Scheme 4. Synthesis of imine compounds **193–199**.

a generated hypothesis, the higher is the entropy with subsequent increase in this cost. The overall cost (total cost) of a hypothesis is calculated by summing over the three cost factors. However, error cost is the main contributor to total cost.

CATALYST also calculates the cost of the null hypothesis, which presumes that there is no relationship in the data and that experimental activities are normally distributed about their mean. Accordingly, the greater the difference from the null hypothesis cost (residual cost, Table C under Supplementary material), the more likely that the hypothesis does not reflect a chance correlation [19,20,22–26]. In a successful automatic modeling run, CATALYST ranks the generated models according to their total costs [22–24].

An additional approach to assess the quality of CATALYST–HYPOGEN pharmacophores is to cross-validate them using the Cat-Scramble algorithm implemented in CATALYST [26,38]. This validation procedure is based on Fisher's randomization test [38]. In this validation test, we selected a 95% confidence level, which instruct CATALYST to generate 19 random spreadsheets by the Cat-Scramble command. Subsequently, CATALYST-HYPOGEN is challenged to use these random spreadsheets to generate hypotheses using exactly the same features and parameters used in generating the initial unscrambled hypotheses [43]. Success in generating pharmacophores of comparable cost criteria to those produced by the original unscrambled data reduces the confidence in the training compounds and the unscrambled original pharmacophore models [26,38]. Based on Fisher randomization criteria, all 120 pharmacophores achieved 95% significance threshold, and were therefore, submitted for subsequent processing (clustering and QSAR analysis).

4.1.6. Clustering of the generated pharmacophore hypotheses

The resulting models (120) were clustered into 26 groups utilizing the hierarchical average linkage method available in CATALYST. Subsequently, the highest-ranking representatives, as judged based on their fit-to-bioactivity correlation values, were selected to represent their corresponding clusters in subsequent QSAR modeling. Table C, under Supplementary material, shows the representative pharmacophores features, success criteria, the corresponding Cat.scramble confidence levels and differences from corresponding null hypotheses.

4.2. QSAR modeling

A set of 96 compounds was employed as the training set for QSAR modeling. The remaining 22 molecules (ca. 20% of the dataset) were employed as an external test subset for validating the QSAR models. The test molecules were selected as follows: the 118 inhibitors were ranked according to their IC_{50} values, then every fifth compound was selected for the test set starting from the high-potency end (Table A under Supplementary material).

The chemical structures of the inhibitors were imported into CERIUS2 as standard 3D single conformers (of the lowest energy within the conformational ensemble generated by CATALYST) representations in SD format. Subsequently, 100 molecular descriptors were calculated for each compound employing the C2.DESCRIPTOR module of CERIUS2. The calculated descriptors included various simple and valence connectivity indices, electro-topological state indices, single point quantum-mechanical descriptors (*via* the AM1 model) and other molecular descriptors (the detailed molecular descriptors are listed under Supplementary material) [40]. Furthermore, the training compounds were fitted against the 26 representative CETP pharmacophore hypotheses, generated by the CATALYST-HYPOGEN automatic runs (shown in Tables A and B), and their fit values (produced by the best-fit command within CATALYST *via* Eq. (5)) were added as additional molecular descriptors.

Genetic function approximation (GFA) was employed to search for the best possible QSAR regression equation capable of

Table 6
The synthesized compounds with their *in vitro* bioactivities.

Synthesized compound[a]	% Inhibition of CETP at 10.0 μM
187	12.6
188	14.8
189	33.8
190	26.3
193	9.8
194	24.9
195	15.4
196	14.9
197	19.5
198	23.7
199	19.9

[a] Compound numbers as in Schemes **3** and **4**.

correlating the variations in biological activities of the training compounds with variations in the generated descriptors, i.e., multiple linear regression modeling (MLR) [40].

Our preliminary diagnostic trials suggested the following optimal GFA parameters: Explore linear equations at mating and mutation probabilities of 50%; population size = 500; number of genetic iterations = 30000 and LOF smoothness parameter = 1.0. However, to determine the optimal number of explanatory terms (QSAR descriptors), it was decided to scan and evaluate all possible QSAR models resulting from 3 to 6 explanatory terms. All QSAR models were validated employing leave-one-out cross-validation (r^2_{LOO}), bootstrapping (r^2_{BS}) [39,40] and predictive r^2 (r^2_{PRESS}) calculated from the test subsets. The predictive r^2_{PRESS} is defined as:[39–42]

$$r^2_{PRESS} = SD - PRESS/SD \quad (6)$$

where SD is the sum of the squared deviations between the biological activities of the test set and the mean activity of the training set molecules, PRESS is the squared deviations between predicted and actual activity values for every molecule in the test set.

4.3. Receiver-operating characteristic (ROC) curve analysis

Selected pharmacophore models (i.e., Hypo4/8, Hypo12/4 and shape-complemented Hypo4/8) were validated by assessing their abilities to selectively capture diverse CETP active compounds from a large testing list of actives and decoys.

The testing list was prepared as described by Verdonk et al. [50,51]. Briefly, decoy compounds were selected based on three basic one-dimensional (1D) properties that allow the assessment of distance (D) between two molecules (e.g., *i* and *j*): (1) the number of hydrogen-bond donors (NumHBD); (2) number of hydrogen-bond acceptors (NumHBA) and (3) count of nonpolar atoms (NP, defined as the summation of Cl, F, Br, I, S and C atoms in a particular molecule). For each active compound in the test set, the distance to the nearest other active compound is assessed by their Euclidean Distance (Eq. (7)):

$$D(i,j) = \sqrt{(\mathrm{NumHBD}_i - \mathrm{NumHBD}_j)^2 + (\mathrm{NumHBA}_i - \mathrm{NumHBA}_j)^2 + (\mathrm{NP}_i - \mathrm{NP}_j)^2} \quad (7)$$

The minimum distances are then averaged over all active compounds (Dmin). Subsequently, for each active compound in the test set, around 33 decoys were randomly chosen from the ZINC database [52]. The decoys were selected in such a way that they did not exceed Dmin distance from their corresponding active compound.

To diversify active members in the list, we excluded any active compound having zero distance ($D(i,j)$) from other active compound(s) in the test set. Active testing compounds were defined as those possessing CETP affinities ranging from 0.0012 to 6.72 μM. The test set included 15 active compounds and 474 ZINC decoys.

The test set (489 compounds) was screened by each particular pharmacophore employing the "Best flexible search" option implemented in CATALYST, while the conformational spaces of the compounds were generated employing the "Fast conformation generation option" implemented in CATALYST. Compounds missing one or more features were discarded from the hit list. In silico hits were scored employing their fit values as calculated by Eq. (5).

The ROC curve analysis describes the sensitivity (Se or true positive rate, Eq. (8)) for any possible change in the number of selected compounds (*n*) as a function of (1-Sp). Sp is defined as specificity or true negative rate (Eq. (9)) [51,53].

$$\mathrm{Se} = \frac{\text{Number of Selected Actives}}{\text{Total Number of Actives}} = \frac{\mathrm{TP}}{\mathrm{TP} + \mathrm{FN}} \quad (8)$$

$$\mathrm{Sp} = \frac{\text{Number of Discarded Inactives}}{\text{Total Number of Inactives}} = \frac{\mathrm{TN}}{\mathrm{TN} + \mathrm{FP}} \quad (9)$$

where, TP is the number of active compounds captured by the virtual screening method (true positives), FN is the number of active compounds discarded by the virtual screening method, TN is the number of discarded decoys (presumably inactives), while FP is the number of captured decoys (presumably inactives).

If all molecules scored by a virtual screening (VS) protocol with sufficient discriminatory power are ranked according to their score (i.e., fit values), starting with the best-scored molecule and ending with the molecule that got the lowest score, most of the actives will have a higher score than the decoys. Since some of the actives will be scored lower than decoys, an overlap between the distribution of active molecules and decoys will occur, which will lead to the prediction of false positives and false negatives [51,53]. An ROC curve is plotted by setting the score of the active molecule as the first threshold. Afterwards, the number of decoys within this cutoff is counted and the corresponding Se and Sp pair is calculated. This calculation is repeated for the active molecule with the second highest score and so forth, until the scores of all actives are considered as selection thresholds.

The ROC curve representing ideal distributions, where no overlap between the scores of active molecules and decoys exists, proceeds from the origin to the upper-left corner until all the actives are retrieved and Se reaches the value of 1. In contrast to that, the ROC curve for a set of actives and decoys with randomly distributed scores tends towards the Se = 1-Sp line asymptotically with increasing number of actives and decoys [51]. The success of a particular virtual screening workflow can be judged from the following criteria (shown in Table 3):

(1) Area under the ROC curve (AUC) [53]. In an optimal ROC curve an AUC value of 1 is obtained; however, random distributions cause an AUC value of 0.5 [51,53].

(2) Overall accuracy (ACC): describes the percentage of correctly classified molecules by the screening protocol (Eq. (10)). Testing compounds are assigned a binary score value of zero (compound not captured) or one (compound captured) [51,54,55].

$$\mathrm{ACC} = \frac{\mathrm{TP} + \mathrm{TN}}{N} = \frac{A}{N} \times \mathrm{Se} + \left(1 - \frac{A}{N}\right) \times \mathrm{Sp} \quad (10)$$

where, *N* is the total number of compounds in the testing database, A is the number of true actives in the testing database.

(3) Overall specificity (SPC): describes the percentage of discarded inactives by the particular virtual screening workflow. Inactive test compounds are assigned a binary score value of zero (compound not captured) or one (compound captured) [51,54,55].

(4) Overall true positive rate (TPR or overall sensitivity): describes the fraction percentage of captured actives from the total number of actives. Active test compounds are assigned a binary score value of zero (compound not captured) or one (compound captured).
(5) Overall false negative rate (FNR or overall percentage of discarded actives): describes the fraction percentage of active compounds discarded by the virtual screening method. Discarded active test compounds are assigned a binary score value of zero (compound not captured) or one (compound captured).

4.4. Addition of shape constraints to pharmacophore models

Shape constraints were added using the CatShape module of CATALYST [18,56]. To generate merged shape-pharmacophore queries for Hypo4/8 and Hypo12/4, the most potent training compound **100** ($IC_{50} = 0.0012$ μM) was first fitted against the pharmacophore models, thereafter, the best-fitted conformer of the inhibitor was used to generate default shape constraints (70%–130% tolerance similarity) that were subsequently merged with each pharmacophore.

4.5. In silico screening of databases for new CETP inhibitors

Shape-complemented Hypo4/8 and combined Hypo4/8–Hypo12/4 were employed as 3D search queries against the NCI and DAC libraries using the "Best Flexible Database Search" option implemented within CATALYST. NCI hits were filtered based on Lipinski's and Veber's rules [46,47]. The remaining hits were fitted against Hypo4/8 and Hypo12/4 using the "best-fit" approach implemented within CATALYST. Subsequently, the fit values together with the relevant molecular descriptors were substituted in QSAR Eq. (1) to predict anti-CETP IC_{50} values. The highest-ranking 52 hits were subsequently tested *in vitro*.

4.6. CETP inhibition assay

4.6.1. Quantification of CETP activity

CETP inhibitory bioactivities were assayed by fluorescent-CE transfer employing commercially available kit (BioVision, Linda Vista Avenue, USA). The assay kit is based on donor molecule containing fluorescent self-quenched neutral lipid that is transferred to an acceptor molecule in the presence of CETP (from rabbit serum). CETP-mediated transfer of the fluorescent neutral lipid to the acceptor molecule results in increase in fluorescence. Inhibition of CETP will prevent lipid transfer and therefore decrease fluorescence intensity.

The assay procedure can be described briefly as follows. An aliquot of 1.5 μL of rabbit serum was added to 160 μL of testing sample. Then 20 μL of the master mix, provided in the assay kit (donor molecule, acceptor molecule and assay buffer), was added, mixed well, and the volume was completed to 203 μL with the provided assay buffer. After incubation at 37 °C for 1 h, fluorescence intensity (Excitation λ: 465 nm; Emission λ: 535 nm) was read in a FLX800TBI Microplate Fluorimeter (BioTek Instruments, Winooski, USA).

4.6.2. Preparation of tested compounds

The tested compounds were initially dissolved in DMSO to yield 10 mM stock solutions and subsequently diluted to the required concentrations using distilled deionized water. The final concentration of DMSO was adjusted to 0.1%. The percentage of residual activity of CETP was determined for each compound by comparing the activity of CETP in the presence and absence of the tested compound. Positive controls were tested to assess the degree of CETP inhibition by 0.1% DMSO. CETP was not affected by DMSO. Negative controls lacking rabbit serum were used as background. All measurements were conducted in duplicates.

4.7. Synthetic procedures

Melting points were measured using Gallenkampf melting point apparatus and are uncorrected. ^{1}H-NMR and ^{13}C-NMR spectra were collected on a Varian Oxford NMR^{300} spectrometer. The samples were dissolved in $CDCl_3$ at a concentration of 0.3–0.7 wt % and placed in 5 mm NMR tubes. Mass spectrometry was performed using LC Mass Bruker Apex-IV mass spectrometer utilizing an electrospray interface.

Infrared spectra were recorded using Shimadzu IRAffinity-1 spectrophotometer. The samples were dissolved in $CHCl_3$ and analysed as thin solid films using NaCl plates. Analytical thin layer chromatography (TLC) was carried out using pre-coated aluminum plates and visualized by UV light (at 254 and/or 360 nm). Elemental analysis was performed using EuroVector elemental analyzer.

Chemicals and solvents were purchased from corresponding companies (Sigma-Aldrich, Riedel-de Haen, Fluka, BDH Laboratory Supplies and Promega Corporation) and were used in the experimentation without further purification.

4.7.1. General procedure for the synthesis of (3-amino-phenyl)-(un)substituted phenyl-methanone ***(175–177)***

3-Aminobenzoic acid **171** (0.411 g, 3 mmol) was dissolved in CH_2Cl_2 (5 mL), and polyphosphoric acid (10 g) was added. Then (un)substituted benzene (6–30 mmol) was added. The mixture was stirred carefully at 80- 180 °C for 3 h and then poured on crushed ice. The solution was carefully made alkaline with 25% ammonia and then extracted with CH_2Cl_2 (3 × 20 mL). The combined extracts were dried on anhydrous Na_2SO_4 and filtrated.

*4.7.1.1. (3-Amino-phenyl)-phenyl-methanone **(175)**.* Evaporation of the solvent gave **175** as a yellow powder (0.23 g, 39%) [48]: mp: 84–86 °C (Lit. mp: 109–109.5 °C); ^{1}H-NMR ($CDCl_3$, δ ppm): 3.82 (bs, 2H, NH_2), 6.88 (d, $J = 7.2$ Hz, 1H), 7.11 (m, 2H), 7.32 (d, $J = 7.2$ Hz, 1H), 7.47 (d, $J = 6.8$ Hz, 2H), 7.56 (d, $J = 6.8$ Hz, 1H), 7.80 (d, $J = 6.8$ Hz, 2H); ^{13}C-NMR ($CDCl_3$, δ ppm): 116.13 (1C), 119.20 (1C), 120.86 (1C), 128.41 (2C), 129.30 (1C), 130.26 (2C), 132.52 (1C), 138.01 (1C), 138.90 (1C), 146.73 (1C), 197.22 (1C); IR (thin film, cm^{-1}): 3480, 3379, 3017, 1651, 1620, 1600, 1490, 1454.

*4.7.1.2. (3-Amino-phenyl)-(4-methoxy-phenyl)-methanone **(176)**.* Evaporation of the solvent gave **176** as a yellow powder (0.35 g, 52%) [48]: mp: 109–111 °C (Lit. mp: 114–116 °C); ^{1}H-NMR ($CDCl_3$, δ ppm): 3.83 (bs, 2H, NH_2), 3.86 (s, 3H, OCH_3), 6.85 (dd, $J = 6.4$, 1.8 Hz, 1H), 6.93 (dd, $J = 6.7$, 2.1 Hz, 2H), 7.05 (dd, $J = 6.4$, 1.8 Hz, 1H), 7.08 (t, $J = 1.8$ Hz, 1H), 7.22 (t, $J = 6.4$ Hz, 1H), 7.81 (dd, $J = 6.7$, 2.1 Hz, 2H); ^{13}C-NMR ($CDCl_3$, δ ppm): 55.72 (1C, OCH_3), 113.69 (2C), 115.94 (1C), 118.69 (1C), 120.39 (1C), 129.20 (1C), 130.53 (1C), 132.77 (2C), 139.59 (1C), 146.75 (1C), 163.37 (1C), 196.05 (1C); IR (thin film, cm^{-1}): 3464, 3364, 3017, 1651, 1613, 1597, 1503, 1475, 1451, 1250.

*4.7.1.3. (3-Amino-phenyl)-biphenyl-4-yl-methanone **(177)**.* The residue, after evaporation of the solvent, was purified by column chromatography eluting with $CHCl_3$/EtOAc (95:5) to give **177** pure as a yellow powder (0.25 g, 30%): mp: 120–122 °C; ^{1}H-NMR ($CDCl_3$, δ ppm): 3.84 (bs, 2H, NH_2), 6.90 (d, $J = 7.6$ Hz, 1H), 7.16 (d, $J = 8.2$ Hz, 2H), 7.26 (t, $J = 7.6$ Hz, 1H), 7.42 (d, $J = 7.0$ Hz, 1H), 7.48 (m, 2H), 7.67 (m, 4H), 7.90 (d, $J = 8.2$ Hz, 2H); ^{13}C-NMR ($CDCl_3$, δ ppm): 114.81 (1C), 117.89 (1C), 119.46 (1C), 125.82 (2C), 126.24 (2C), 127.11 (1C), 127.91 (2C), 128.05 (1C), 129.67 (2C), 135.37 (1C), 137.77 (1C), 138.96 (1C), 144.03 (1C), 145.52 (1C), 195.55 (1C); IR (thin film, cm^{-1}): 3427, 3399, 3021, 1651, 1608, 1601, 1515, 1451, 1458.

4.7.2. General procedure for the synthesis of (4-amino-phenyl)-(un)substituted phenyl-methanone ***(180–182)***

4-Aminobenzoic acid **178** (0.411 g, 3 mmol) was dissolved in CH_2Cl_2 (5 mL), and polyphosphoric acid (10 g) was added. Then (un)substituted benzene (6–30 mmol) was added. The mixture was stirred carefully at 80–190 °C for 3 h and then poured on crushed ice. The solution was carefully made alkaline with 25% ammonia and then extracted with CH_2Cl_2 (3 × 20 mL). The combined extracts were dried on anhydrous Na_2SO_4 and filtrated.

4.7.2.1. (4-Amino-phenyl)-phenyl-methanone ***(180)*** *[48].* Evaporation of the solvent gave **180** as a yellow powder (0.24 g, 41%) [48]: mp: 120–122 °C (Lit. mp: 106–110 °C); ^{1}H-NMR ($CDCl_3$, δ ppm): 4.19 (bs, 2H, NH_2), 6.66 (m, 2H), 7.46 (m, 2H), 7.53 (m, 2H), 7.70 (m, 3H); ^{13}C-NMR ($CDCl_3$, δ ppm): 113.86 (2C), 127.57 (1C), 128.31 (2C), 129.72 (2C), 131.65 (1C), 133.18 (2C), 139.11 (1C), 151.25 (1C), 195.58 (1C); IR (thin film, cm^{-1}): 3495, 3406, 3017, 1636, 1615, 1597, 1510, 1448.

4.7.2.2. (4-Amino-phenyl)-biphenyl-4-yl-methanone ***(181)****.* The residue, after evaporation of the solvent, was purified by column chromatography eluting with $CHCl_3$/MeOH (99:1) to give **181** pure as a yellow powder (0.31 g, 38%): mp: 198–200 °C; ^{1}H-NMR ($CDCl_3$, δ ppm): 4.15 (bs, 2H, NH_2), 6.69 (dd, $J = 8.4$, 1.8 Hz, 2H), 7.43 (m, 5H), 7.67 (m, 4H), 7.79 (m, 2H); ^{13}C-NMR ($CDCl_3$, δ ppm): 112.64 (2C), 125.76 (2C), 126.24 (2C), 126.57 (1C), 126.93 (1C), 127.89 (2C), 129.18 (2C), 131.87 (2C), 136.51 (1C), 139.21 (1C), 143.23 (1C), 149.86 (1C), 193.87 (1C); IR (thin film, cm^{-1}): 3433, 3341, 3021, 1652, 1613, 1597, 1539, 1448.

4.7.2.3. (4-Amino-phenyl)-(2,4-dimethoxy-phenyl)-methanone ***(182)****.* Evaporation of the solvent gave **182** as a yellow powder (0.69 g, 89%): mp: 164–166 °C; ^{1}H-NMR ($CDCl_3$, δ ppm): 3.72 (s, 3H, OCH_3), 3.84 (s, 3H, OCH_3), 4.14 (bs, 2H, NH_2), 6.50 (s, 1H), 6.53 (dd, $J = 7.6$, 2.4 Hz, 1H), 6.60 (dd, $J = 6.7$, 1.9 Hz, 2H), 7.29 (dd, $J = 7.6$, 0.9 Hz, 1H), 7.65 (dd, $J = 6.7$, 1.9 Hz, 2H); ^{13}C-NMR ($CDCl_3$, δ ppm): 55.71 (1C, OCH_3), 55.86 (1C, OCH_3), 99.07 (1C), 104.48 (1C), 113.72 (2C), 122.71 (1C), 128.89 (1C), 131.37 (1C), 132.79 (2C), 151.23 (1C), 159.10 (1C), 162.67 (1C), 194.26 (1C); IR (thin film, cm^{-1}): 3435, 3356, 3020, 1651, 1610, 1597, 1503, 1455, 1277, 1215.

4.7.3. General procedure for the synthesis of benzylidene-aminophenyl-methanone compounds ***(187–190, 193–199)***

One of the aminobenzophenone intermediates (**175–177, 180–182**) (3 mmol) was dissolved in cyclohexane (20–25 mL). Then (un)substituted benzaldehyde (7.5 mmol) was added. The mixture was refluxed at 85–90 °C for 3 h and then poured on crushed ice and cooled. The resulting suspension was filtered, and washed with cold aqueous ethanol (50%).

4.7.3.1. [3-(Benzylidene-amino)-phenyl]-(4-methoxy-phenyl)-methanone ***(187)****.* The residue was purified by column chromatography using $CHCl_3$/MeOH (99:1) as eluent, to afford the title compound **187** as yellow oil (0.66 g, 70%): $R_f = 0.50$ ($CHCl_3$-MeOH, 97:3); ^{1}H-NMR ($CDCl_3$, δ ppm): 3.87 (s, 3H, OCH_3), 6.83 (dd, $J = 7.9$, 2.3 Hz, 1H), 6.86 (dd, $J = 7.9$, 2.3 Hz, 1H), 6.94 (dd, $J = 6.9$, 2.1 Hz, 2H), 7.07 (t, $J = 7.9$ Hz, 1H), 7.10 (t, $J = 2.3$ Hz, 1H), 7.21 (t, $J = 8.4$ Hz, 1H), 7.28 (dd, $J = 8.4$, 2.4 Hz, 2H), 7.35 (dd, $J = 8.4$, 2.4 Hz, 2H), 7.82 (dd, $J = 6.9$, 2.1 Hz, 2H), 8.41 (s, 1H, N=CH); ^{13}C-NMR ($CDCl_3$, δ ppm): 55.72 (1C, OCH_3), 111.71 (1C), 113.70 (2C), 115.71 (1C), 115.95 (1C), 118.69 (1C), 119.89 (1C), 120.46 (2C), 120.93 (1C), 129.31 (2C), 130.53 (1C), 131.85 (1C), 132.77 (2C), 149.59 (1C), 161.72 (1C), 163.37 (1C), 196.05 (1C); IR (thin film, cm^{-1}): 1717, 1643, 1597, 1505, 1489, 1454, 1250; MS (ESI, negative mode): m/z $[M + Na]^+$ 338.11625 ($C_{21}H_{17}NNaO_2$ requires 338.12593).

4.7.3.2. {3-[(4-Methoxy-benzylidene)-amino]-phenyl}-(4-methoxy-phenyl)-methanone ***(188)****.* The residue was purified by crystallization from petroleum ether to afford the title compound **188** as a white powder (0.26 g, 25%): $R_f = 0.90$ ($CHCl_3$-MeOH, 97:3); mp: 77–78 °C; ^{1}H-NMR ($CDCl_3$, δ ppm): 3.87 (s, 3H, OCH_3), 3.89 (s, 3H, OCH_3), 6.98 (m, 4H), 7.41 (dd, $J = 7.6$, 1.5 Hz, 1H), 7.48 (t, $J = 7.6$ Hz, 1H), 7.55 (dd, $J = 7.6$, 1.5 Hz, 1H), 7.58 (t, $J = 1.5$ Hz, 1H), 7.86 (m, 4H), 8.41 (s, 1H, N=CH); ^{13}C-NMR ($CDCl_3$, δ ppm): 55.69 (1C, OCH_3), 55.74 (1C, OCH_3), 113.84 (2C), 114.48 (2C), 121.85 (1C), 125.10 (1C), 127.07 (1C), 129.20 (1C), 129.23 (1C), 130.34 (1C), 130.92 (2C), 132.77 (2C), 139.57 (1C), 152.55 (1C), 160.88 (1C), 162.71 (1C), 163.51 (1C), 195.60 (1C); IR (thin film, cm^{-1}): 1721, 1651, 1601, 1574, 1512, 1458, 1254, 1165; MS (ESI, positive mode): m/z $[M + H]^+$ 346.14377 ($C_{22}H_{20}NO_3$ requires 346.13649); Anal. Calcd for $C_{22}H_{19}NO_3$: C 76.50, H 5.54, N 4.06, found: C 76.33, H 5.45, N 3.68.

4.7.3.3. Biphenyl-4-yl-{3-[(3-trifluoromethyl-benzylidene)-amino]-phenyl}-methanone ***(189)****.* The residue was purified by column chromatography using $CHCl_3$/EtOAc (99:1) as eluent, to afford the title compound **189** as a light-brown powder (0.58 g, 45%): $R_f = 0.63$ ($CHCl_3$-MeOH, 97:3); mp: 119–120 °C; ^{1}H-NMR ($CDCl_3$, δ ppm): 7.32 (d, $J = 7.2$ Hz, 1H), 7.46 (d, $J = 8.3$ Hz, 2H), 7.51 (t, $J = 7.2$ Hz, 1H), 7.62 (d, $J = 7.8$ Hz, 1H), 7.71 (m, 2H), 7.80 (dd, $J = 7.8$, 2.7 Hz, 4H), 7.86 (d, $J = 8.1$ Hz, 1H), 7.97 (d, $J = 8.1$ Hz, 2H), 8.08 (d, $J = 8.3$ Hz, 2H), 8.23 (s, 1H), 8.54 (s, 1H, N=CH); ^{13}C-NMR ($CDCl_3$, δ ppm): 119.29 (1C), 120.96 (1C), 123.25 (1C), 126.47 (2C), 127.77 (1C), 128.34 (2C), 129.09 (1C), 129.87 (2C), 130.11 (1C), 130.43 (2C), 131.78 (2C), 132.69 (2C), 135.21 (1C), 135.88 (1C), 137.56 (1C), 138.78 (1C), 144.16 (1C), 145.23 (1C), 155.52 (1C), 160.35 (1C), 195.46 (1C); IR (thin film, cm^{-1}): 1721, 1651, 1601, 1582, 1485, 1454; MS (ESI, positive mode): m/z $[M + H]^+$ 430.14133 ($C_{27}H_{19}F_3NO$ requires 430.13405); Anal. Calcd for $C_{27}H_{18}F_3NO$: C 75.52, H 4.22, N 3.26, found: C 75.47, H 4.24, N 3.23.

4.7.3.4. Phenyl-{3-[(4-trifluoromethyl-benzylidene)-amino]-phenyl}-methanone ***(190)****.* The residue was purified by crystallization from petroleum ether to afford the title compound **190** as a white powder (0.11 g, 10%): $R_f = 0.67$ ($CHCl_3$-MeOH, 97:3); mp: 90–92 °C; ^{1}H-NMR ($CDCl_3$, δ ppm): 7.49 (dd, $J = 2.0$, 0.6 Hz, 1H), 7.52 (dd, $J = 7.6$, 2.0 Hz, 2H), 7.61 (dd, $J = 7.8$, 1.5 Hz, 1H), 7.65 (t, $J = 7.6$ Hz, 1H), 7.70 (dd, $J = 7.8$, 1.5 Hz, 2 H), 7.74 (d, $J = 8.2$ Hz, 2H), 7.84 (dd, $J = 7.8$, 1.5 Hz, 2H), 8.03 (d, $J = 8.2$ Hz, 2H), 8.55 (s, 1H, N=CH); ^{13}C-NMR ($CDCl_3$, δ ppm): 121.99 (1C), 125.56 (1C), 126.01 (1C), 126.06 (1C), 128.36 (1C), 128.62 (2C), 129.35 (2C), 129.45 (1C), 130.02 (2C), 130.32 (2C), 132.86 (1C), 137.63 (1C), 139.03 (1C), 151.71 (1C), 159.89 (1C), 159.92 (1C), 196.56 (1C); IR (thin film, cm^{-1}): 1722, 1651, 1601, 1574, 1500, 1462; MS (ESI, negative mode): m/z M^+ 353.10330 ($C_{21}H_{14}F_3NO$ requires 353.10275); Anal. Calcd for $C_{21}H_{14}F_3NO$: C 71.38, H 3.99, N 3.96, found: C 71.32, H 3.81, N 3.86.

4.7.3.5. Biphenyl-4-yl-{4-[(3-trifluoromethyl-benzylidene)-amino]-phenyl}-methanone ***(193)****.* The residue was purified by crystallization from petroleum ether to afford the title compound **193** as an off-white powder (0.21 g, 16%): $R_f = 0.74$ ($CHCl_3$-MeOH, 97:3); mp: 165–166 °C; ^{1}H-NMR ($CDCl_3$, δ ppm): 7.30 (d, $J = 8.4$ Hz, 2H), 7.43 (d, $J = 7.0$ Hz, 1H), 7.50 (t, $J = 7.6$ Hz, 2H), 7.66 (m, 3H), 7.73 (d, $J = 8.4$ Hz, 2H), 7.79 (d, $J = 7.6$ Hz, 1H), 7.92 (m, 4H), 8.11 (d, $J = 7.9$ Hz, 1H), 8.23 (s, 1H), 8.54 (s, 1H, N=CH); ^{13}C-NMR ($CDCl_3$, δ ppm): 120.88 (2C), 125.93 (1C), 127.25 (2C), 127.55 (2C), 128.45 (2C), 128.52 (1C), 129.22 (2C), 129.68 (1C), 130.84 (2C), 131.82 (2C), 132.42 (1C), 132.43 (1C), 135.67 (1C), 136.67 (1C), 136.72 (1C), 140.22 (1C), 145.41 (1C), 155.35 (1C), 160.15 (1C), 195.74 (1C); IR (thin film, cm^{-1}): 1720, 1643, 1601, 1580, 1435; MS (ESI, positive mode): m/z $[M + H]^+$ 430.14133 ($C_{27}H_{19}F_3NO$ requires 430.13405);

Anal. Calcd for $C_{27}H_{18}F_3NO$: C 75.52, H 4.22, N 3.26, found: C 75.42, H 4.26, N 3.26.

*4.7.3.6. {4-[(4-tert-Butyl-benzylidene)-amino]-phenyl}-(2,4-dimethoxy-phenyl)-methanone **(194)**.* The residue was purified by crystallization from diethyl ether to afford the title compound **194** as a yellow powder (0.12 g, 10%):) $R_f = 0.65$ ($CHCl_3$-MeOH, 97:3); mp: 139–141 °C; ^{1}H-NMR ($CDCl_3$, δ ppm): 1.36 (s, 9H, 3 × CH_3), 3.73 (s, 3H, OCH_3), 3.88 (s, 3H, OCH_3), 6.52 (d, $J = 2.2$ Hz, 1H), 6.56 (dd, $J = 8.4$, 2.2 Hz, 1H), 7.18 (dd, $J = 6.7$, 1.9 Hz, 2H), 7.41 (d, $J = 8.4$ Hz, 1H), 7.51 (dd, $J = 6.7$, 1.9 Hz, 2H), 7.84 (m, 4H), 8.43 (s, 1H, N═CH); ^{13}C-NMR ($CDCl_3$, δ ppm): 31.41 (3C, CH_3), 35.34 (1C), 55.76 (1C, OCH_3), 55.82 (1C, OCH_3), 99.05 (1C), 104.77 (1C), 120.64 (2C), 122.03 (1C), 126.08 (2C), 129.12 (2C), 131.43 (2C), 132.20 (1C), 133.49 (1C), 136.15 (1C), 155.78 (1C), 156.30 (1C), 159.64 (1C), 161.56 (1C), 163.42 (1C), 195.00 (1C); IR (thin film, cm^{-1}): 1724, 1651, 1589, 1566, 1504, 1462, 1273, 1211; MS (ESI, positive mode): m/z $[M+H]^+$ 402.20637 ($C_{26}H_{28}NO_3$ requires 402.19909); Anal. Calcd for $C_{26}H_{27}NO_3$: C 77.78, H 6.78, N 3.49, found: C 77.73, H 6.79, N 3.17.

*4.7.3.7. (2,4-Dimethoxy-phenyl)-{4-[(4-trifluoromethyl-benzylidene)-amino]-phenyl}-methanone **(195)**.* The residue was purified by crystallization from petroleum ether to afford the title compound **195** as an off-white-yellowish powder (0.32 g, 26%): $R_f = 0.70$ ($CHCl_3$-MeOH, 97:3); mp: 102–104 °C; ^{1}H-NMR ($CDCl_3$, δ ppm): 3.72 (s, 3H, OCH_3), 3.88 (s, 3H, OCH_3), 6.52 (d, $J = 2.1$ Hz, 1H), 6.57 (dd, $J = 8.5$, 2.3 Hz, 1H), 7.22 (dd, $J = 6.6$, 1.8 Hz, 2H), 7.42 (d, $J = 8.5$ Hz, 1H), 7.75 (d, $J = 8.2$ Hz, 2H), 7.85 (dd, $J = 6.6$, 1.8 Hz, 2H), 8.04 (d, $J = 8.2$ Hz, 2H), 8.51 (s, 1H, N═CH); ^{13}C-NMR ($CDCl_3$, δ ppm): 55.78 (1C, OCH_3), 55.81 (1C, OCH_3), 99.05 (1C), 104.85 (1C), 120.63 (2C), 121.82 (1C), 125.97 (1C), 126.07 (2C), 129.42 (2C), 131.43 (2C), 132.32 (1C), 136.95 (1C), 139.10 (1C), 139.11 (1C), 155.16 (1C), 159.71 (1C), 159.95 (1C), 163.58 (1C), 194.89 (1C); IR (thin film, cm^{-1}): 1721, 1651, 1601, 1574, 1501, 1462, 1308, 1277; MS (ESI, positive mode): m/z $[M+H]^+$ 414.13115 ($C_{23}H_{19}F_3NO_3$ requires 414.12388); Anal. Calcd for $C_{23}H_{18}F_3NO_3$: C 66.86, H 4.39, N 3.39, found: C 66.04, H 4.28, N 3.34.

*4.7.3.8. (2,4-Dimethoxy-phenyl)-{4-[(3-trifluoromethyl-benzylidene)-amino]-phenyl}-methanone **(196)**.* The residue was purified by crystallization from petroleum ether to afford the title compound **196** as an off-white powder (0.61 g, 49%): $R_f = 0.67$ ($CHCl_3$-MeOH, 97:3); mp: 79–80 °C; ^{1}H-NMR ($CDCl_3$, δ ppm): 3.73 (s, 3H, OCH_3), 3.88 (s, 3H, OCH_3), 6.52 (d, $J = 2.3$ Hz, 1H), 6.57 (dd, $J = 8.5$, 2.3 Hz, 1H), 7.21 (dd, $J = 6.5$, 1.9 Hz, 2H), 7.42 (d, $J = 8.5$ Hz, 1H), 7.62 (t, $J = 7.7$ Hz, 1H), 7.76 (d, $J = 7.7$ Hz, 1H), 7.84 (dd, $J = 6.5$, 1.9 Hz, 2H), 8.09 (d, $J = 7.7$ Hz, 1H), 8.21 (s, 1H), 8.51 (s, 1H, N═CH); ^{13}C-NMR ($CDCl_3$, δ ppm): 55.78 (1C, OCH_3), 55.80 (1C, OCH_3), 99.04 (1C), 104.85 (1C), 120.62 (2C), 121.84 (1C), 125.80 (1C), 125.85 (1C), 128.38 (1C), 129.64 (1C), 131.44 (2C), 131.48 (1C), 132.31 (1C), 132.39 (1C), 136.78 (1C), 136.89 (1C), 155.17 (1C), 159.71 (1C), 159.86 (1C), 163.56 (1C), 194.90 (1C); IR (thin film, cm^{-1}): 1719, 1651, 1601, 1505, 1458, 1331, 1277; MS (ESI, positive mode): m/z $[M+H]^+$ 414.13115 ($C_{23}H_{19}F_3NO_3$ requires 414.12388); Anal. Calcd for $C_{23}H_{18}F_3NO_3$: C 66.86, H 4.39, N 3.39, found: C 66.93, H 4.34, N 3.23.

*4.7.3.9. (2,4-Dimethoxy-phenyl)-{4-[(4-methoxy-benzylidene)-amino]-phenyl}-methanone **(197)**.* The residue was purified by crystallization from petroleum ether to afford the title compound **197** as an off-white powder (0.12 g, 11%): $R_f = 0.61$ ($CHCl_3$-MeOH, 97:3); mp: 127–128 °C; ^{1}H-NMR ($CDCl_3$, δ ppm): 3.72 (s, 3H, OCH_3), 3.88 (s, 3H, OCH_3), 3.89 (s, 3H, OCH_3), 6.52 (d, $J = 2.3$ Hz, 1H), 6.57 (dd, $J = 8.5$, 2.3 Hz, 1H), 6.99 (dd, $J = 6.8$, 2.1 Hz, 2H), 7.18 (dd, $J = 6.7$, 2.1 Hz, 2H), 7.41 (d, $J = 8.5$ Hz, 1H), 7.82 (dd, $J = 6.8$, 2.1 Hz, 2H), 7.86 (dd, $J = 6.7$, 2.1 Hz, 2H), 8.39 (s,1H, N═CH); ^{13}C-NMR ($CDCl_3$, δ ppm): 55.70 (1C, OCH_3), 55.77 (1C, OCH_3), 55.82 (1C, OCH_3), 99.05 (1C), 104.76 (1C), 114.51 (2C), 120.69 (2C), 122.06 (1C), 129.15 (1C), 131.06 (2C), 131.45 (2C), 132.17 (1C), 135.99 (1C), 156.36 (1C), 159.63 (1C), 160.93 (1C), 162.85 (1C), 163.39 (1C), 195.00 (1C); IR (thin film, cm^{-1}): 1721, 1647, 1601, 1574, 1512, 1308, 1254; MS (ESI, positive mode): m/z $[M+H]^+$ 376.15433 ($C_{23}H_{22}NO_4$ requires 376.14706); Anal. Calcd for $C_{23}H_{21}NO_4$: C 73.58, H 5.64, N 3.73, found: C 73.12, H 5.67, N 4.23.

*4.7.3.10. (2,4-Dimethoxy-phenyl)-{4-[(3-methoxy-benzylidene)-amino]-phenyl}-methanone **(198)**.* The residue was purified by crystallization from petroleum ether to afford the title compound **198** as a yellow powder (0.29 g, 26%): $R_f = 0.83$ ($CHCl_3$-MeOH, 97:3); mp: 48–50 °C; ^{1}H-NMR ($CDCl_3$, δ ppm): 3.73 (s, 3H, OCH_3), 3.86 (s, 3H, OCH_3), 3.89 (s, 3H, OCH_3), 6.52 (m, 4H), 7.19 (d, $J = 8.2$ Hz, 1H), 7.29 (d, $J = 8.2$ Hz, 1H), 7.53 (s, 1H), 7.66 (d, $J = 8.5$ Hz, 2H), 7.83 (d, $J = 8.5$ Hz, 2H), 8.43 (s,1H, N═CH); ^{13}C-NMR ($CDCl_3$, δ ppm): 55.69 (1C, OCH_3), 55.74 (1C, OCH_3), 55.84 (1C, OCH_3), 99.06 (1C), 104.63 (1C), 112.18 (1C), 113.73 (2C), 119.04 (1C), 120.65 (1C), 122.78 (2C), 131.40 (1C), 132.24 (1C), 132.79 (2C), 137.50 (1C), 151.12 (1C), 159.11 (1C), 160.27 (1C), 161.62 (1C), 162.67 (1C), 194.23 (1C); IR (thin film, cm^{-1}): 1721, 1651, 1597, 1505, 1462, 1312, 1277; MS (ESI, positive mode): m/z $[M+Na]^+$ 398.13628 ($C_{23}H_{21}NNaO_4$ requires 398.14706), Anal. Calcd for $C_{23}H_{21}NO_4$: C 73.58, H 5.64, N 3.73, found: C 73.22, H 5.69, N 3.92.

*4.7.3.11. {4-[(4-Methoxy-benzylidene)-amino]-phenyl}-phenyl-methanone **(199)**.* The residue was purified by crystallization from diethyl ether to afford the title compound **199** as a yellowish-orange powder (0.17 g, 18%): $R_f = 0.68$ ($CHCl_3$-MeOH, 97:3); mp: 114–116 °C; ^{1}H-NMR ($CDCl_3$, δ ppm): 3.89 (s, 3H, OCH_3), 7.00 (dd, $J = 6.7$, 2.1 Hz, 2H), 7.24 (dd, $J = 6.7$, 2.1 Hz, 2H), 7.51 (dd, $J = 6.5$, 1.5 Hz, 2H), 7.57 (dd, $J = 6.0$, 1.8 Hz, 1H), 7.81 (dd, $J = 6.0$, 1.8 Hz, 2H), 7.87 (m, 4H), 8.40 (s, 1H, N═CH); ^{13}C-NMR ($CDCl_3$, δ ppm): 55.72 (1C, OCH_3), 114.54 (2C), 120.91 (2C), 128.49 (2C), 129.09 (1C), 130.13 (2C), 131.13 (2C), 131.87 (2C), 132.39 (1C), 134.63 (1C), 138.25 (1C), 156.54 (1C), 161.17 (1C), 162.94 (1C), 196.23 (1C); IR (thin film, cm^{-1}): 1721, 1651, 1601, 1574, 1512, 1447, 1254; MS (ESI, positive mode): m/z $[M+H]^+$ 316.13321 ($C_{21}H_{18}NO_2$ requires 316.12593); Anal. Calcd for $C_{21}H_{17}NO_2$: C 79.98, H 5.43, N 4.44, found: C 79.39, H 5.45, N 4.47.

Acknowledgments

This project was partially sponsored by the Faculty of Graduate Studies (Ph.D. Thesis of Reema Abu Khalaf). The authors wish to thank the Deanship of Scientific Research and Hamdi-Mango Center for Scientific Research at the University of Jordan for their generous funds. The authors are also indebted to national cancer institute for freely providing hit molecules for evaluation.

Appendix. Supplementary material

Supplementary data associated with this article can be found in the online version, at doi:10.1016/j.ejmech.2009.12.070.

References

[1] G.K. Hansson, Inflammation, atherosclerosis, and coronary artery disease. N. Engl. J. Med. 352 (2005) 1685–1695.
[2] B. Lamarche, J.P. Despres, S. Moorjani, B. Cantin, G.R. Dagenais, P.J. Lupien, Triglycerides and HDL-cholesterol as risk factors for ischemic heart disease, Results from the Quebec cardiovascular study. Atherosclerosis 119 (1996) 235–245.
[3] A.R. Tall, N. Wang, P. Mucksavage, Is it time to modify the reverse cholesterol transport model? J. Clin. Invest 108 (2001) 1273–1275.

[4] X. Qiu, A. Mistry, M.J. Ammirati, B.A. Chrunyk, R.W. Clark, Y. Cong, J.S. Culp, D.E. Danley, T.B. Freeman, K.F. Geoghegan, M.C. Griffor, S.J. Hawrylik, C.M. Hayward, P. Hensley, L.R. Hoth, G.A. Karam, M.E. Lira, D.B. Lloyd, K.M. McGrath, K.J. Stutzman-Engwall, A.K. Subashi, T.A. Subashi, J.F. Thompson, I.K. Wang, H. Zhao, A.P. Seddon, Crystal structure of cholesteryl ester transfer protein reveals a long tunnel and four bound lipid molecules. Nat. Struct. Mol. Biol. 14 (2007) 106–113.
[5] S.M. Boekholdt, J.A. Kuivenhoven, N.J. Wareham, R.J.G. Peters, J.W. Jukema, R. Luben, S.A. Bingham, N.E. Day, J.J.P. Kastelein, K.T. Khaw, Plasma levels of cholesteryl ester transfer protein and the risk of future coronary artery disease in apparently healthy men and women. Circulation 110 (2004) 1418–1423.
[6] R. McPherson, C.J. Mann, A.R. Tall, M. Hogue, L. Martin, R.W. Milne, Y.L. Marcel, Plasma concentration of cholesteryl ester transfer protein in hyperlipoproteinemia. Arterioscler. Thromb 11 (1991) 797–804.
[7] M.S. Castilho, S. Marcelo, R.V.C. Guido, A.D. Andricopulo, 2D Quantitative structure–activity relationship studies on a series of cholesteryl ester transfer protein inhibitors. Bioorg. Med. Chem. 15 (2007) 6242–6252.
[8] P. Hanumantharao, S.V. Sambasivarao, L.K. Soni, A.K. Gupta, S.G. Kaskhedikar, QSAR analysis of analogs of bis[2-(acylamino) Ph] disulfides, 2-(acylamino) benzenethiols and S-[2-(acylamino) Ph] alkanethioates as antihyperlipidemic agents. Ind. J. Chem., Sect. B, Org. Chem. Includ. Med. Chem. 44B (2005) 1481–1486.
[9] M.A. Kelkar, D.V. Pednekar, S.R. Pimple, K.G. Akamanchi, 3D QSAR studies of inhibitors of cholesterol ester transfer protein (CETP) by CoMFA, CoMSIA and GFA methodologies. Med. Chem. Res. 13 (2004) 590–604.
[10] M.T.D. Cronin, T.W. Schultz, Pitfalls in QSAR. J. Mol. Struct. (Theochem.) 622 (2003) 39–51.
[11] M. Akamatsu, Current state and perspectives of 3D-QSAR. Curr. Top. Med. Chem. 12 (2002) 1381–1394.
[12] M.O. Taha, Y. Bustanji, M. Al-Ghussein, M. Mohammad, H. Zalloum, I.M. Al-Masri, N. Atallah, Pharmacophore modeling, quantitative structure–activity relationship analysis, and in-silico screening reveal potent glycogen synthase kinase-3beta inhibitory activities for cimetidine, hydroxychloroquine, and gemifloxacin. J. Med. Chem. 51 (2008) 2062–2077.
[13] I.M. Al-masri, K. Mohammad, M.O. Taha, Discovery of DPP IV inhibitors by pharmacophore modeling and QSAR analysis followed by in silico screening. Chem. Med. Chem. 3 (11) (2008) 1763–1779.
[14] M.O. Taha, L.A. Dahabiyeh, Y. Bustanji, H. Zalloum, S. Saleh, Combining ligand-based pharmacophore modeling, QSAR analysis and in-silico screening for the discovery of new potent hormone sensitive lipase inhibitors. J. Med. Chem. 51 (2008) 6478–6494.
[15] M.O. Taha, N. Atallah, A.G. Al-Bakri, C. Paradis-Bleau, H. Zalloum, K. Younis, R.C. Levesque, Discovery of new MurF Inhibitors via pharmacophore modeling and QSAR analysis followed by in silico screening. Bioorg. Med. Chem. 16 (2008) 1218–1235.
[16] M.O. Taha, Y. Bustanji, A.G. Al-Bakri, M. Yousef, W.A. Zalloum, I.M. Al-Masri, N. Atallah, Discovery of new potent human protein tyrosine phosphatase inhibitors via pharmacophore and QSAR analysis followed by in silico screening. J. Mol. Graphics Model 25 (2007) 870–884.
[17] A.M. Abu Hammad, M.O. Taha, Pharmacophore modeling, quantitative structure–activity relationship analysis, and shape-complemented in silico screening allow access to novel influenza neuraminidase inhibitors. J. Chem. Inf. Model. 49 (2009) 978–996.
[18] Catalyst User Guide. Accelrys Software Inc., San Diego, CA, 2005.
[19] P.W. Sprague, R. Hoffmann, in: H. Van de Waterbeemd, B. Testa, G. Folkers (Eds.), CATALYST Pharmacophore Models and Their Utility As Queries for Searching 3D Databases, Current Tools for Medicinal Chemistry, VHCA, Basel, 1997, pp. 223–240.
[20] D. Barnum, J. Greene, A. Smellie, P.J. Sprague, Identification of Common Functional configurations among molecules. Chem. Inf. Comput. Sci. 36 (1996) 563–571.
[21] A. Smellie, S. Teig, P. Towbin, Poling: promoting conformational variation. J. Comput. Chem. 16 (1995) 171–187.
[22] H. Li, J. Sutter, R. Hoffmann, in: O.F. Guner (Ed.), Pharmacophore Perception, Development, and Use in Drug Design, International University Line, California, 2000, pp. 173–189.
[23] J. Sutter, O.F. Guner, R. Hoffmann, H. Li, M. Waldman, Effect of Variable Weights and Tolerances on Predictive Model Generation, Pharmacophore Perception, Development, and Use in Drug Design. International University Line, California, 2000, pp. 501–511.
[24] Y. Kurogi, O.F. Guner, Pharmacophore modeling and three-dimensional database searching for drug design using catalyst. Curr. Med. Chem. 8 (2001) 1035–1055.
[25] I.B. Bersuker, S. Bahçeci, J.E. Boggs, Pharmacophore Perception, Development, and Use in Drug Design. in: O.F. Gűner (Ed.). International University Line, California, 2000, pp. 457–473.
[26] K. Poptodorov, T. Luu, R. Hoffmann, in: T. Langer, R.D. Hoffmann (Eds.), Methods and Principles in Medicinal Chemistry, Pharmacophores and Pharmacophores Searches, Wiley-VCH, Weinheim 2, 2006, pp. 17–47.
[27] J. Singh, C.E. Chuaqui, P.A. Boriack-Sjodin, W.C. Lee, T. Pontz, M.J. Corbley, H.K. Cheung, R.M. Arduini, J.N. Mead, M.N. Newman, J.L. Papadatos, S. Bowes, S. Josiah, L.E. Ling, Successful shape-based virtual screening: the discovery of a potent inhibitor of the type I TGFβ receptor kinase (TβRI). Bioorg. Med. Chem. Lett. 13 (2003) 4355–4359.
[28] M.O. Taha, A.M. Qandil, D.D. Zaki, M.A. AlDamen, Ligand-based assessment of factor Xa binding site flexibility via elaborate pharmacophore exploration and genetic algorithm-based QSAR modeling. Eur. J. Med. Chem. 40 (2005) 701–727.
[29] P.A. Keller, M. Bowman, K.H. Dang, J. Garner, S.P. Leach, R. Smith, A.J. McCluskey, Pharmacophore development for corticotropin-releasing hormone: new insights into inhibitor activity. J. Med. Chem. 42 (1999) 2351–2357.
[30] R.G. Karki, V.M. Kulkarni, A feature based pharmacophore for Candida albicans MyristoylCoA: protein N-myristoyltransferase inhibitors. Eur. J. Med. Chem. 36 (2001) 147–163.
[31] M.O. Taha, A.G. Al-Bakri, W.A. Zalloum, Discovery of potent inhibitors of pseudomonal quorum sensing via pharmacophore modeling and In silico screening. Bioorg. Med. Chem. Lett. 16 (2006) 5902–5906.
[32] K. Moffat, V.J. Gillet, M. Whittle, G. Bravi, A.R. Leach, A comparison of field-based similarity searching methods, CatShape, FBSS, and ROCS. J. Chem. Inf. Model 48 (2008) 719–729.
[33] R.C. Durley, M.L. Grapperhaus, M.A. Massa, D.A. Mischke, B.L. Parnas, Y.M. Fobian, N.P. Rath, D.D. Honda, M. Zeng, D.T. Connolly, D.M. Heuvelman, B.J. Witherbee, K.C. Glenn, E.S. Krul, M.E. Smith, J.A. Sikorski, Discovery of chiral N, N-disubstituted trifluoro-3-amino-2-propanols as potent inhibitors of cholesteryl ester transfer protein. J. Med. Chem. 43 (2000) 4575–4578.
[34] M.A. Massa, D.P. Spangler, R.C. Durley, B.S. Hickory, D.T. Connolly, B.J. Witherbee, M.E. Smith, J.A. Sikorski, Novel heteroaryl replacements of aromatic 3-tetrafluoroethoxy substituents in trifluoro-3-(tertiary amino)-2-propanols as potent inhibitors of cholesteryl ester transfer protein. Bioorganic. Med. Chem. Lett. 11 (2001) 1625–1628.
[35] R.C. Durley, M.L. Grapperhaus, B.S. Hickory, M.A. Massa, J.L. Wang, D.P. Spangler, D.A. Mischke, B.L. Parnas, Y.M. Fobian, N.P. Rath, D.D. Honda, M. Zeng, D.T. Connolly, D.M. Heuvelman, B.J. Witherbee, M.A. Melton, K.C. Glenn, E.S. Krul, M.E. Smith, J.A. Sikorski, Chiral *N,N*-disubstituted trifluoro-3-amino-2-propanols are potent inhibitors of cholesteryl ester transfer protein. J. Med. Chem. 45 (2002) 3891–3904.
[36] E.J. Reinhard, J.L. Wang, R.C. Durley, Y.M. Fobian, M.L. Grapperhaus, B.S. Hickory, M.A. Massa, M.B. Norton, M.A. Promo, M.B. Tollefson, W.F. Vernier, D.T. Connolly, B.J. Witherbee, M.A. Melton, K.J. Regina, M.E. Smith, J.A. Sikorski, Discovery of a simple picomolar inhibitor of cholesteryl ester transfer protein. J. Med. Chem. 46 (2003) 2152–2168.
[37] R.P. Sheridan, S.K. Kearsley, Why do we need so many chemical similarity search methods? Drug Discov. Today 7 (2002) 903–911.
[38] R. Fisher, in: The Principle of Experimentation Illustrated by a Psycho-Physical ExpeHafner Publishing Co, eighth ed. Hafner Publishing, New York, 1966.
[39] A. Tropsha, P. Gramatica, V.K. Gombar, Quant. structure–activity relationship. Comb. Sci. 22 (2003) 69–77.
[40] CERIUS2 QSAR Users' Manual. Accelrys Inc., San Diego, CA, 2005.
[41] F.P. Maguna, M.B. Nunez, N.B. Okulik, E.A. Castro, Methodologies QSAR/QSPR/QSTR: current state and perspectives. Int. J. Chem. Model 1 (2) (2009) 221–243.
[42] L.F. Ramsey, W.D. Schafer, in: The Statistical Sleuth, first ed. Wadesworth Publishing Company, USA, 1997.
[43] E.M. Krovat, T. Langer, Non-peptide angiotensin ii receptor antagonists: chemical feature based pharmacophore identification. J. Med. Chem. 46 (2003) 716–726.
[44] L.B. Kier, L.H. Hall, in: J. Devillers, A.T. Balaban (Eds.), Topological Indices and Related Descriptors in QSAR and QSPR, Gordon and Breach, London, 1999, pp. 491–562.
[45] S.W. Homans, Water, water everywhere — except where it matters? Drug Discov. Today 12 (2007) 534–539.
[46] C.A. Lipinski, F. Lombardo, B.W. Dominy, P.J. Feeney, Experimental and computational approaches to estimate solubility and permeability in drug discovery and development settings. Adv. Drug Del. Rev. 46 (2001) 3–26.
[47] D.F. Veber, S.R. Johnson, H.Y. Cheng, B.R. Smith, K.W. Ward, K.D. Kopple, Molecular properties that influence the oral bioavailability of drug candidates. J. Med. Chem. 45 (2002) 2615–2623.
[48] I. Ivanov, S. Nikolova, S. Statkova-Abeghe, Efficient one-pot friedel–crafts acylation of benzene and its derivatives with unprotected aminocarboxylic acids in polyphosphoric acid. Synth. Commun. 36 (2006) 1405–1411.
[49] V. del Amo, D. Philp, Making imines without making water-exploiting a recognition-mediated Aza-Wittig reaction. Org. Lett. 11 (2009) 301–304.
[50] M.L. Verdonk, L. Marcel, V. Berdini, M.J. Hartshorn, W.T.M. Mooij, C.W. Murray, R.D. Taylor, P. Watson, Virtual screening using protein-ligand docking: avoiding artificial enrichment. J. Chem. Inf. Comput. Sci. 44 (2004) 793–806.
[51] J. Kirchmair, P. Markt, S. Distinto, G. Wolber, T. Langer, Evaluation of the performance of 3D virtual screening protocols: RMSD comparisons, enrichment assessments, and decoy selection—what can we learn from earlier mistakes? J. Comput. Aided. Mol. Des. 22 (2008) 213–228.
[52] J.J. Irwin, B.K. Shoichet, ZINC – a free database of commercially available compounds for virtual screening. J. Chem. Inf. Comput. Sci. 45 (2005) 177–182.
[53] N. Triballeau, F. Acher, I. Brabet, J.P. Pin, H.O. Bertrand, Virtual screening workflow development guided by the "receiver-operating characteristic" curve approach. application to high-throughput docking on metabotropic glutamate receptor subtype 4. J. Med. Chem. 48 (2005) 2534–2547.
[54] M. Jacobsson, P. Liden, E. Stjernschantz, H. Bostroem, U. Norinder, Improving structure-based virtual screening by multivariate analysis of scoring data. J. Med. Chem. 46 (2003) 5781–5789.
[55] H. Gao, C. Williams, P. Labute, J. Bajorath, Binary quantitative structure–activity relationship (QSAR) analysis of estrogen receptor ligands. J. Chem. Inf. Comput. Sci. 39 (1999) 164–168.
[56] M. Hahn, Three-dimensional shape-based searching of conformationally flexible compounds. J. Chem. Inf. Comput. Sci. 37 (1997) 80–86.